

DETECTION OF ULTRAVIOLET HALOS AROUND HIGHLY INCLINED GALAXIES

EDMUND HODGES-KLUCK¹ & JOEL N. BREGMAN¹

submitted to ApJ

ABSTRACT

We report the discovery of diffuse ultraviolet light around late-type galaxies out to 5–20 kpc from the midplane using *Swift* and *GALEX* images. The emission is consistent with the stellar outskirts in the early-type galaxies but not in the late-type galaxies, where the emission is quite blue and consistent with a reflection nebula powered by light escaping from the galaxy and scattering off dust in the halo. Our results agree with expectations from halo dust discovered in extinction by Ménard et al. (2010) to within a few kpc of the disk and imply a comparable amount of hot and cold gas in galaxy halos (a few $\times 10^8 M_{\odot}$ within 20 kpc) if the dust resides primarily in Mg II absorbers. The results also highlight the potential of UV photometry to study individual galaxy halos.

Keywords: galaxies: halos — ISM: dust, extinction — ultraviolet: galaxies

1. INTRODUCTION

The composition and masses of galaxy halos are important predictions of galaxy formation and evolution models. Material can be ejected from the disk into the halo through galactic winds (stellar feedback) or winds and jets driven by active galactic nuclei (AGN), and fresh material can fall into the halo from the circumgalactic medium (CGM). Both of these processes are thought to occur in the lives of normal galaxies, but the relative contribution of each process over cosmic time is unclear as they both produce hot and cold components that occupy roughly the same space.

One of the most striking examples of similar looking halos produced by very different processes concerns the “missing baryon problem” (Bregman 2007). Galaxies (and even groups and some clusters of galaxies) are “missing” a substantial fraction of the baryons they are expected to have from the cosmic baryon fraction if the baryons all cooled onto the disk. There are two basic possibilities for Schechter (1976) L_* galaxies: either the baryons might all have cooled onto the galactic disk before most of them were expelled by stellar feedback, or most baryons have been prevented from accreting onto the disk, having been heated to the virial temperature (a few million degrees) on infall. Both scenarios produce extended hot halos, and the cooling rate is slow enough for the gas to reach hydrostatic equilibrium. Thus, neither gas temperature nor the surface brightness profile distinguishes the scenarios. However, the gas metallicity is dispositive, as gas that has cycles through the disk is enriched with metals from stellar mass loss and supernovae (SNe).

The situation is similar for the cool components. In L_* and smaller halos, accretion of fresh material from the CGM can occur through cool flows, but tidal interactions with other galaxies (especially satellites) can also produce cool streams in the halo (for a review, see Putman et al. 2012), and cool clouds such as the high velocity clouds may be produced by a “galactic fountain”

powered by SNe in the disk (Bregman 1980). It is not generally possible to determine the origin of cool halo gas through where it is detected, and again the metallicity is a good way to distinguish between different scenarios. In some galaxies, it is also possible to map the spatial and velocity structure of the cool gas, but this technique requires very deep H I exposures that are only feasible for nearby large systems (e.g., Oosterloo et al. 2007; Westmeier et al. 2007).

While metallicity is an important and unambiguous indicator of halo gas history, it is hard to measure because the halo gas is tenuous and therefore faint. There are only a few “normal” galaxies with X-ray halos that are sufficiently bright to make a measurement in the hot halo (of which the brightest is NGC 891; Hodges-Kluck & Bregman 2013), and measurements in the cooler gas rely on absorption lines in the continua of background quasars (e.g., the COS-Halos survey; Tumlinson et al. 2013). The quasar absorption-line method has been very productive, but it suffers from important limitations. First, there are few galaxies with more than one bright quasar behind the halo, so we are limited to a statistical view. Second, the cross-section to background quasars is very small close to the galaxy, so our view of the halo between 5–20 kpc is limited, and this is the region where we expect interaction between stellar feedback and accreted components in the halo. Third, making these measurements requires long exposures to get a high signal-to-noise ratio (S/N) in the spectrum.

Recently, Ménard et al. (2010, MSFR10) discovered that quasars are reddened by dust extinction in galaxy halos out to 1 Mpc from the galaxy (evidence for dust extinction out to 200 kpc towards two background galaxies was first reported by Zaritsky 1994). This dust is evidently a distinct component from the well known extraplanar dusty clouds near the disk, which form filamentary structures that do not extend beyond a few kpc from the disk and are likely related to the disk–halo cycle (e.g., Rossa et al. 2004; Howk 2009). The discovery of dust at large radii suggests that halo gas may be observable through its dust content apart from the extinction towards background quasars, since the dust will also emit in the mid-infrared band and scatter ambient photons.

Electronic address: hodgeskl@umich.edu

¹ Department of Astronomy, University of Michigan, Ann Arbor, MI 48109

Table 1
Properties of *Galex* and *Swift* UVOT Filters Used

Instrument	Filter	λ_{eff} Å	$\Delta\lambda_{\text{FWHM}}$ Å	Pixel Scale (arcsec pixel ⁻¹)	FWHM psf (arcsec)	Flux Conversion (erg cm ⁻² Hz)
UVOT	UVW1	2600	693	0.502	2.37 ^a	$9.524 \times 10^{-28\text{a}}$
Galex	NUV	2267	616	1.5	5.3 ^c	$3.529 \times 10^{-28\text{b}}$
UVOT	UVM2	2246	498	0.502	2.45 ^a	$1.396 \times 10^{-27\text{a}}$
UVOT	UVW2	1928	657	0.502	2.92 ^a	$8.225 \times 10^{-28\text{a}}$
Galex	FUV	1516	269	1.5	4.2 ^c	$1.073 \times 10^{-28\text{b}}$

References. — (a) Breeveld et al. (2010) (b) Poole et al. (2008) (c) Morrissey et al. (2007)

Note. — Note that the *uvw1* and *uvw2* filters have red leaks, making their effective wavelengths source dependent.

Diffuse intergalactic dust has also been discovered in galaxy clusters using the same method (Chelouche et al. 2007; McGee & Balogh 2010).

Diffuse dust emission is only visible within several kpc of the disk because of the high IR background (e.g., Howk 2009), although a few polycyclic aromatic hydrocarbon features were detected to above 6 kpc around NGC 5907 (Irwin & Madden 2006), and Burgdorf et al. (2007) find continuum dust emission up to a similar height. Also, McCormick et al. (2013) found extraplanar PAH emission to 6 kpc in galactic winds. However, dust extinction is most efficient in the ultraviolet where the sky is also quite dark. In the UV band, the scattering albedo (the proportion of scattering to the total extinction, which comprises scattering and absorption) is around 0.5 (e.g., Draine 2003), so we might expect to detect this dust as reflection nebulas around highly inclined, star-forming galaxies. This idea is similar to seeing (in the Earth’s atmosphere) the beam of a searchlight that is pointed away from the observer.

The reflection nebula luminosity depends on the UV luminosity of the galaxy, escape fraction of UV photons from the disk, and the type and quantity of the dust. The reflection nebula spectrum depends on the grain composition and size, which in turn is tied to the gas metallicity, as many of the metals in the interstellar medium are depleted onto grains Jenkins (2004); Draine (2004). If the metallicity of the dust-bearing gas can be measured, one can place a lower bound on the metallicity of the halo gas with some estimate of the gas mass (N_H , hot gas mass, or a known dust-to-gas ratio). Motivated by this possibility, we searched for reflection nebulas in the NUV and FUV bands around highly inclined, star-forming galaxies to measure a photometric SED.

In this paper, we present initial results for a sample of these galaxies with both *Swift* Ultraviolet and Optical Telescope (UVOT) and *Galaxy Evolution Explorer* (*GALEX*) archival data where we have detected UV halos out to 5–20 kpc around late-type galaxies. Our main result is the detection of the halos, which we attribute to dust-scattered light. These halos are seen around every galaxy in the sample (and many more that are not included in the present work). With the existing data, we cannot constrain the metallicity of the gas, but with better spectral coverage (especially in the far UV), dust models using different proportions of silicate and carbonaceous grains can be distinguished (e.g., the models in Nozawa & Fukugita 2013). The detection of the halos is important in its own right because if they trace cold,

dust-bearing gas, the comparatively high resolution of UV imaging can isolate halo gas with much less integration time than is required for high resolution 21-cm interferometry.

The remainder of this paper is organized as follows: in Section 2 we describe the sample of galaxies and data processing, then we discuss instrumental scattered-light artifacts in Section 3. In Section 4 we present our results and describe some basic trends. In Section 5 we use the spectral information to argue that the light comes from a reflection nebula around late-type galaxies, and in Section 6 we find that the amount of light is consistent with extrapolating the MSFR10 extinction profile to near the disk. In Section 7 we briefly discuss the implications of our work. Throughout this paper, we use the dust models of Weingartner & Draine (2001) (hereafter, WD01), but note that others exist.

2. SAMPLE, INSTRUMENTS, AND DATA PROCESSING

Although the scattering cross-section is highest in the UV, the column densities are low, so we expect to see a small fraction of the UV light that leaks into the halo. Our sample therefore consists of nearby, highly inclined, star-forming galaxies that are luminous in the *B*-band in regions of low UV background.

Our choice of instruments is motivated by the UV filters aboard *Swift* and *GALEX* and the abundance of archival data for each. If UV halos exist, they are evidently faint (as they have not previously been reported), so systematic instrumental issues (such as scattered light artifacts and filter defects) are important. The UV foreground is also variable, so comparing multiple exposures from different epochs is useful. Thus, we also restricted our sample to galaxies with both UVOT and *GALEX* data to compare any halos detected in either instrument (and to give us as many points as possible for an SED).

In this section, we describe the UVOT and *GALEX* filters, our sample criteria, and our data processing methods. Part of our processing includes removing instrumental artifacts from the UVOT exposures, which is described in the following section.

2.1. *GALEX* and *Swift*-UVOT Filters

GALEX is a 50 cm telescope that obtains near UV (NUV) and far UV (FUV) images simultaneously in a wide (1.2° diameter) field of view (Martin et al. 2005; Morrissey et al. 2007). The NUV filter is a wide-band filter covering 1700–3000 Å with a peak effective area at around 2200 Å and an angular resolution of 5.3 arcsec.

Table 2
Basic Parameters of Galaxies in this Work

Name	Type	i (deg)	d (Mpc)	M_K (mag)	$E(B - V)$ mag	$B - V$ (mag)	M_* ($10^{10} M_\odot$)	SFR _{IR} ($M_\odot \text{ yr}^{-1}$)
	(1)	(2)	(3)	(4)	(5)	(6)	(7)	(8)
ESO 243-049	S0	90	91	-24.1	0.011	-	-	-
IC 5249	SBcd	90	29.5	-19.8	0.030	0.95	0.15	-
NGC 24	Sc	70.1	9.1	-20.6	0.017	0.48	0.15	0.11
NGC 527	S0a	90	76.3	-24.4	0.024	-	-	-
NGC 891	SBb	88	10.0	-24.0	0.057	0.70	5.0	2.4
NGC 1426	E4	90	22.7	-23.0	0.014	0.87	2.6	-
NGC 2738	Sbc	66.1	45.5	-23.8	0.029	-	-	-
NGC 2765	S0	90	50	-24.3	0.029	-	-	-
NGC 2841	Sb	68	14.1	-24.6	0.013	0.79	9.6	<0.48
NGC 2974	E4	90	24.7	-25.7	0.048	0.93	32.	<0.45
NGC 3079	SBcd	82.5	16.5	-23.7	0.010	0.53	2.8	6.1
NGC 3384	E-S0	90	11.8	-23.5	0.024	0.88	4.1	-
NGC 3613	E6	90	29.5	-24.3	0.011	0.90	8.7	-
NGC 3623	SABa	90	12.6	-24.4	0.022	0.92	10.	-
NGC 3628	Sb	79.3	11.3	-24.4	0.024	0.68	7.0	4.8
NGC 3818	E5	90	36.1	-23.9	0.031	0.91	6.0	-
NGC 4036	S0	90	20.8	-24.0	0.021	0.85	6.2	<0.32
NGC 4088	SABc	71	16.2	-23.6	0.017	0.69	2.8	2.8
NGC 4173	SBcd	90	7.8	-18.2 ^a	0.018	-	-	-
NGC 4388	Sb	82	17.1	-23.0	0.029	0.57	1.4	2.2
NGC 4594	Sa	78.5	9.8	-24.9	0.046	0.88	15.	0.28
NGC 5301	SBc	90.0	23.9	-22.7	0.015	0.55	1.1	1.0
NGC 5775	SBc	83.2	26.7	-24.4	0.037	0.66	6.8	6.9
NGC 5866	S0a	90	15.3	-24.0	0.011	0.78	5.3	0.81
NGC 5907	SABc	90	16.6	-24.0	0.009	0.62	4.4	1.9
NGC 6503	Sc	73.5	5.3	-21.2	0.028	0.58	0.31	0.15
NGC 6925	Sbc	84.1	30.7	-24.4	0.052	0.57	5.6	2.8
NGC 7090	SBc	90	6.3	-20.6	0.020	0.45	0.14	0.14
NGC 7582	SBab	68.2	23.0	-24.4	0.012	0.66	6.7	13
UGC 6697	Sm	90	96.6	-24.1	0.019	0.25	2.5	<5.6
UGC 11794	Sab	78.0	75.4	-23.7	0.092	-	-	<5.2

Note. — Cols. (1) Morphological type and (2) Disk Inclination angle (taken from the HyperLeda galaxy database available at <http://leda.univ-lyon1.fr>) (3) Distance in Mpc taken from NED (<http://nedwww.ipac.caltech.edu>), either using the average redshift-independent distance or the redshift distance in WMAP cosmology (4) 2MASS Extended Source Catalog (Skrutskie et al. 2006) absolute K-band magnitude (5) Foreground Galactic extinction from NED (Schlafly & Finkbeiner 2011) (6) The extinction- and redshift-corrected $B - V$ color from HyperLeda (7) Stellar masses computed from M_K and color corrections from Bell & de Jong (2001) (8) Star formation rate estimated from the Kennicutt (1998) relation $\text{SFR} = 4.5 \times 10^{-44} L_{\text{IR}} M_\odot \text{ yr}^{-1}$. L_{IR} we measure as defined by Rice et al. (1988) $L_{\text{IR}} = 5.67 \times 10^5 d_{\text{Mpc}}^2 (13.48 f_{12} + 5.16 f_{25} + 2.58 f_{60} + f_{100}) L_\odot$, where the fluxes at 12, 25, 60, and 100 μm are in Jy from the IRAS catalog (<http://irsa.ipac.caltech.edu/Missions/iras.html>)

^a NGC 4173 is not in any 2MASS catalogs, so we measured this from the 2MASS K -band image.

The FUV filter covers 1400–1800Å and has a peak effective area at 1500Å, with an angular resolution of 4.3 arcsec. Additional properties are listed in Table 1.

The UVOT (Roming et al. 2005) is one of three instruments aboard the *Swift* observatory (Gehrels et al. 2004) and collects data simultaneously with the other instruments. The UVOT has a much smaller ($17 \times 17 \text{ arcmin}^2$) field of view but a higher (~ 1 arcsec) angular resolution and filters extending from 1600–8000Å. In this paper, we use only the UV filters (*uvw1*, *uvw2*, and *uvw3*). A summary of their properties is given in Table 1.

The *uvw1* and *uvw2* filters have “red tails” in their effective area curves², meaning that a portion of the measured flux comes from the optical band. Thus, the effective wavelengths in these filters are higher than their nominal wavelengths by an amount that depends on the source spectrum. This can be seen in Figure 1, where we show the effective area curves for the UVOT and *GALEX* filters in the top panel along with arbitrarily scaled UV spectra of template E/S0 and Sbc galaxies

from Coleman et al. (1980). It is clear that the effective wavelength for early-type galaxies is higher than for late-type systems. Applying a correction to measure only the true UV fluxes requires knowledge of the intrinsic spectrum (in this case the galaxy halo), which has not previously been measured. The nature of this correction can be used to help determine the underlying spectrum in combination with the *GALEX* and *uvw2* filters, which we discuss in Section 5.

Although we do not know the underlying halo spectrum, the red tail is much smaller in the *uvw2* than *uvw1* filter, and the FUV and *uvw2* fluxes bracket the *uvw2* and provide a useful constraint on the real UV flux. There are two basic possibilities for the halo emission: a stellar halo or reflection nebula (discussed in detail in Section 5), but in either case the correction to the *uvw2* flux, constrained by the other filters, is constrained enough to apply a correction to the reported fluxes. We do not correct the *uvw1* fluxes, where the effective wavelength is a much stronger function of the underlying spectrum (but see Section 5).

To correct the *uvw2* flux we use a template-based method similar to those in Brown et al. (2010) and

² see http://heasarc.gsfc.nasa.gov/docs/swift/analysis/uvot_digest/redtail.html

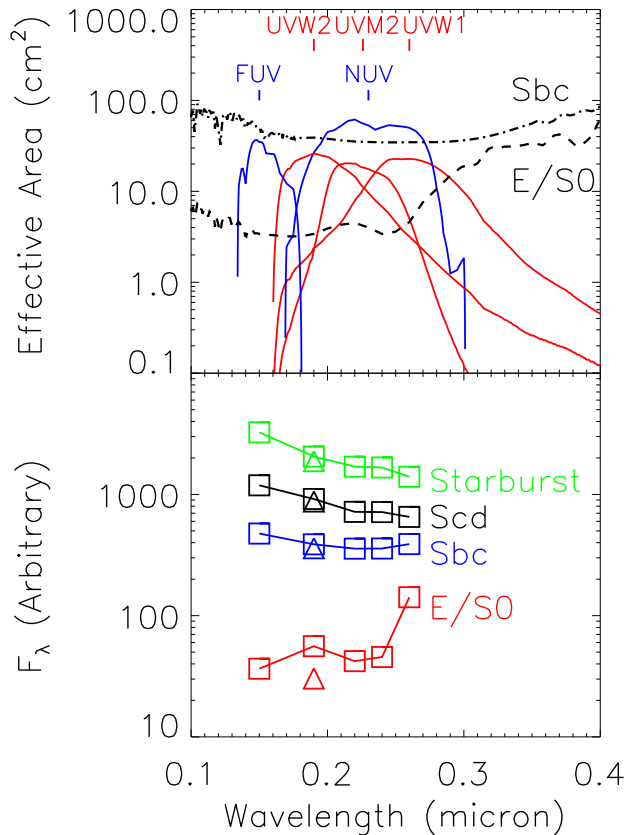


Figure 1. *Top:* *GALEX* and UVOT effective area curves for each filter with Sbc and E/SO templates from Bolzonella et al. (2000) overlaid with arbitrary units. The red tails of the *uvw2* and *uvw1* move the effective wavelength of the filters to longer wavelengths, depending on the spectrum. *Bottom:* SEDs for four template galaxies in the *GALEX* and UVOT filters. The triangles denote the corrected *uvw2* flux when the filter response is clipped at 0.24 micron.

Tzanavaris et al. (2010). We use the template galaxy spectra from Coleman et al. (1980) (as updated by Bolzonella et al. 2000) and Kinney et al. (1996) and the filter effective area curves, and measure the *uvw2* flux below 2400Å. The *uvw2* flux density is

$$F_{uvw2} = \frac{\int F_{\lambda} A_{\text{eff}}(\lambda) d\lambda}{\int A_{\text{eff}}(\lambda) d\lambda}, \quad (1)$$

so the correction factor c_{uvw2} is the ratio of F_{uvw2} computed using a *uvw2* response cut off at 2400Å (rest-frame) and all wavelengths. The lower panel of Figure 1 shows the *GALEX*+UVOT SEDs for several templates with the corrected *uvw2* fluxes shown as triangles. c_{uvw2} ranges from 0.6–1.0 depending on the galaxy template. E/SO galaxies have $c_{uvw2} = 0.55 - 0.65$, whereas spirals of type Sb or later have $c_{uvw2} = 0.90 - 0.97$. We adopt correction factors of $c_{uvw2} = 0.60$ for elliptical galaxies, 0.65 for S0 galaxies, 0.80 for type Sa galaxies, and 0.93 for all late-type galaxies. We apply the same corrections to the halo fluxes.

2.2. Sample Criteria

We used the HyperLeda database³ to define a sample of candidate galaxies that are within 50 Mpc, have an inclination of $i \gtrsim 65^\circ$, and $M_B < -19$ mag. These criteria were guided by the need to spatially resolve the halo in galaxies with a large intrinsic UV brightness. The “inclination” of the early-type galaxies refers to the projected elongation.

The working sample consists of galaxies on this list with good *Swift* and *GALEX* data. For most galaxies, we require at least 1000s of exposure time in each UV filter except *uvw1*. All of the data we use are archival, so there is a wide range in exposure times. We also included a few galaxies at larger distances with deep *Swift* data to determine the limits of our ability to detect halos.

The sample was further culled by excluding interacting galaxies with tidal tails and those that contain or are near very bright point sources (or bright starbursts) that might produce instrumental scattered-light rings (Section 3). We also excluded galaxies such as M82 with galactic winds that are clearly visible in the halo, galaxies that are too large (a major axis larger than ~ 10 arcmin, such as for NGC 4945) to define meaningful background regions on the UVOT chip, and galaxies in regions of bright or visibly structured “cirrus” (scattered UV emission from dust in our Galaxy) on scales relevant to measuring a flat background. In a few cases, we are able to use emission from one side of a galaxy but not the other. Cirrus emission is all-sky, but for most of the galaxies in the working sample the surrounding region has approximately uniform foreground emission. Finally, we omit some galaxies for idiosyncratic reasons such as instrumental artifacts, proximity of the target to another extended object, or very crowded fields.

These criteria leave us with 30 galaxies with sufficient spectral coverage to measure a 4-point SED, and we also include NGC 7090 because of its very deep *uvw2* data, but do not use it for most of the analysis. There are many other galaxies with either *Swift* or *GALEX* data, but not both; as our major goal is to search for halo emission, we require both instruments to identify instrumental issues.

The basic properties of the sample are listed in Table 2, where we have used values from HyperLeda and the NASA/IPAC Extragalactic Database⁴ along with the mass-to-light ratio of Bell & de Jong (2001) and IR star formation law of Kennicutt (1998) to estimate the stellar masses and star formation rate (SFR). The M_K values were obtained from the 2MASS archive⁵, whereas the SFR was computed using IRAS fluxes⁶. The inclinations for some galaxies are suspect, and inclinations reported for early-type galaxies may not be meaningful. The total good exposure times in each UV filter are given in Table 3.

Since we are using archival data from a variety of programs, the sample is not complete in any metric, and includes a variety of distances, inclinations, SFR, and galaxy morphologies. Still, most of the galaxies have $M_K \sim -24$ mag and are roughly Milky Way sized. Many of the galaxies are in the *GALEX* Ultraviolet Atlas of Nearby Galaxies (Gil de Paz et al. 2007), but the au-

³ <http://leda.univ-lyon1.fr/>

⁴ <http://ned.ipac.caltech.edu/>

⁵ <http://irsa.ipac.caltech.edu/applications/2MASS/PubGalPS/>

⁶ <http://irsa.ipac.caltech.edu/Missions/iras.html>

Table 3
Total Useful UV Exposure Times

Name	UVOT			Gallex	
	<i>uvw1</i> (s)	<i>uvm2</i> (s)	<i>uvw2</i> (s)	NUV (s)	FUV (s)
ESO 243-049	5459	8304	28463	13214	7966
IC 5249	-	8784	7716	4467	1705
NGC 24	8208	9298	9247	1577	1577
NGC 527	817	2052	2738	1532	1632
NGC 891	9787	15353	15200	6283	6047
NGC 1426	10640	5904	10736	1696	1696
NGC 2738	253	453	563	3203	3203
NGC 2765	3958	17204	11843	1693	1693
NGC 2841	873	1128	1744	14387	10723
NGC 2974	-	6767	16543	2694	2694
NGC 3079	-	8512	1185	16108	16108
NGC 3384	560	768	1118	1667	1667
NGC 3613	4851	12637	9105	1680	1680
NGC 3623	3193	7122	5300	1656	1656
NGC 3628	1579	1728	3059	17076	5812
NGC 3818	2853	8497	10616	1166	1166
NGC 4036	1643	1713	2512	2445	2438
NGC 4088	-	17781	8031	3493	3493
NGC 4173	2161	1908	2353	1648	1648
NGC 4388	6234	7242	10792	4994	2538
NGC 4594	1027	1354	2055	1917	1917
NGC 5301	578	880	1129	4657	1549
NGC 5775	4181	23678	14979	5346	2776
NGC 5866	1052	1428	2109	1526	1526
NGC 5907	9722	2695	14484	5423	1544
NGC 6503	-	12598	6546	6502	2431
NGC 6925	1259	18355	13360	1835	1677
NGC 7090	-	19697	2646	-	-
NGC 7582	5060	406	544	4817	4817
UGC 6697	2451	2552	1972	2915	2915
UGC 11794	821	639	3228	4551	4551

Note. — The total exposure time is the total amount of good time in the combined images we used for each filter.

thors did not examine the halo emission.

2.3. Data Processing

The archival *GALEX* data were retrieved⁷ as fully reduced datasets, and for most galaxies we did no further processing. The *GALEX* data reduction pipeline is described in (Morrissett et al. 2007). For our analysis, we use the reduced intensity maps but not the background-subtracted versions. The background files provided by the *GALEX* pipeline are not adequate for detecting diffuse emission (Sujatha et al. 2010).

Even in the intensity maps that include the background, the background is not flat because the images are flat fielded based on forcing observations of the standard white dwarf LDS 749B to be uniform everywhere on the chip. However, the main source of NUV background is the zodiacal light, which is redder than the standard star⁸. It is difficult to correct this in post-processing because the *GALEX* field of view virtually always contains some Galactic cirrus with spatial variations on similar scales. Because the UVOT field of view is much smaller than the *GALEX* field, as long as the galaxy is within a region where the background varies slowly we do not need to correct the entire field.

The *Swift* data⁹ were reprocessed from the most basic data product (a list of events and telemetry information

or raw images) so that we could combine exposures from within a single observation and between observations to achieve a high S/N . This is required for almost every *Swift* dataset because in order to study the evolution of gamma-ray burst afterglow SEDs, a single *Swift*/UVOT observation typically consists of a large number of shorter exposures in several of the available filters.

To create the each analysis image, we first reduced and calibrated each exposure in the observations. We mostly followed the processing flowchart in the UVOT Software User’s Guide¹⁰, and applied the latest calibrations described in Breeveld et al. (2010, 2011)¹¹. This includes the correction for large-scale sensitivity variations. Breeveld et al. (2010) note that for point source photometry, the large-scale sensitivity correction should not be applied directly to the image. However, for extended diffuse emission it is necessary to do so. We also added a few steps that are described in Section 3 to remove persistent scattered light artifacts. Finally, we summed and exposure corrected all the good data. It is important to note that because the background varies between exposures, exposure correction does not produce a uniform sensitivity where there is imperfect overlap, and we reject exposures with backgrounds much higher than the average. We used the USNO-B1.0 star catalog (Monet et al. 2003) to compute the astrometry for each exposure individually and to verify the final image.

We masked point sources outside the galaxies using the tool UVOTDETECT, which is based on the SExtractor code (Bertin & Arnouts 1996). Many point sources are bright at longer wavelengths but fade in the far UV, so we used a very conservative mask generated from the NUV to minimize contamination from undetected point sources in the FUV. We excised detected point sources out to 90% of encircled energy based on the latest psf calibration available¹² and used the nominal psf FWHM in each filter to exclude undetected point sources seen in other filters. For very bright sources, we used a larger mask.

3. UV BACKGROUND AND SCATTERED LIGHT ARTIFACTS

In most cases, our measured fluxes (Section 4) are 2–50% of the background. Detecting halo emission requires averaging over many pixels to improve the S/N and measuring the systematic error in the background, which is dominated by real spatial variation. This variation can be due to Galactic cirrus, instrumental scattered light, or, as in the *GALEX* NUV, due to the flat-fielding issue when the background is dominated by zodiacal light (zodiacal light itself is not spatially variable in the field of view).

The diffuse scattered light artifacts are the most significant obstacle to detecting halo flux with the UVOT because they occur in every exposure, cover most of the chip, vary with position, and have a comparable or greater “surface brightness” than the halo flux. However, some of these artifacts have a persistent and predictable nature and can be subtracted.

⁷ <http://galex.stsci.edu/GR6/>

⁸ <http://www.galex.caltech.edu/researcher/techdoc-ch4.html>

⁹ <http://heasarc.nasa.gov/docs/swift/archive/>

¹⁰ see Figure 2.1 in http://archive.stsci.edu/swiftuvot/UVOT_swguide.v2.2.pdf

¹¹ see also <http://heasarc.gsfc.nasa.gov/docs/heasarc/caldb/swift/docs/uvot/>

¹² <http://heasarc.gsfc.nasa.gov/docs/heasarc/caldb/swift/docs/uvot/>

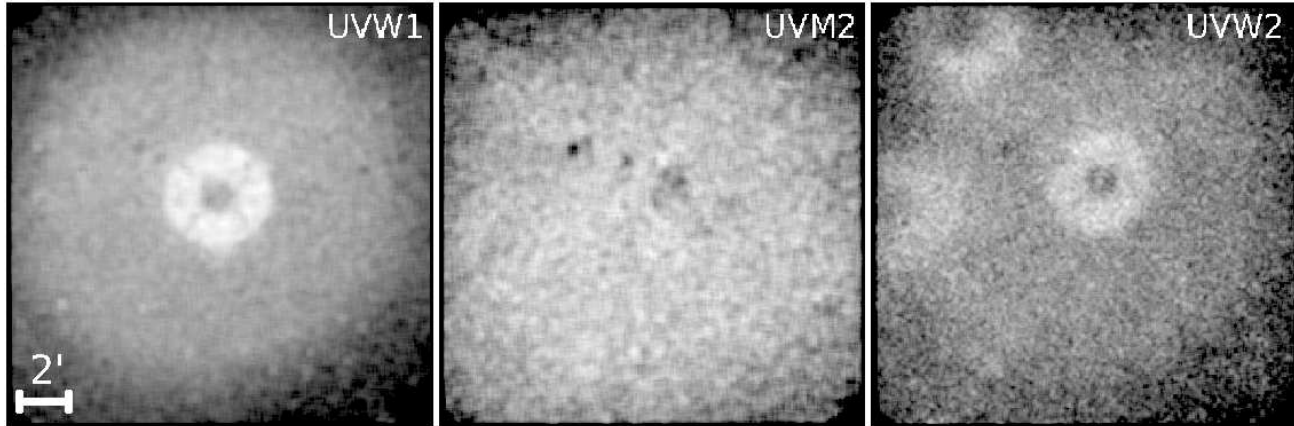


Figure 2. Images of the persistent scattered-light artifacts in the UVOT filters. The images were generated by stacking many deep exposures after removing point sources and processing up through flat-fielding and exposure correction, and are in detector coordinates. The final images have been lightly smoothed. Each of the visible rings has an outer radius of 2 arcmin.

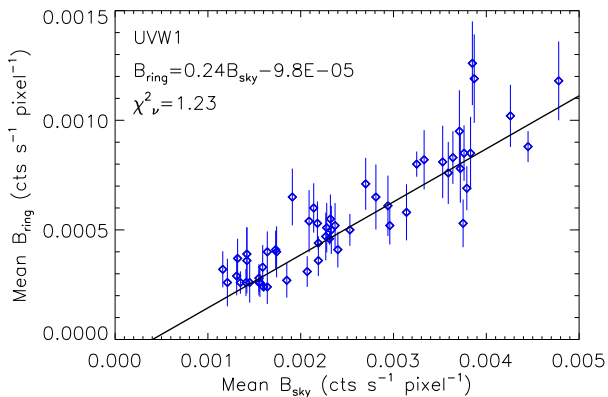


Figure 3. The background-subtracted surface brightness the central ring of the *uvw1* filter pattern B_{ring} as a function of the sky background measured near the chip edges B_{sky} . The relation appears to be linear in each UVOT filter. Most observations used in our sample have a *uvw1* $B_{\text{sky}} \sim 0.002$ counts s^{-1} pixel $^{-1}$.

In this section, we describe the background and foreground components, the scattered light artifacts and our methods to mitigate them, and the remaining systematic uncertainty in the background, which dominates the uncertainty in our flux measurements. Finally, we discuss the potential for contamination by diffuse scattered light artifacts associated with individual stars (and, by extension, extended sources).

3.1. Background and Foreground Components

The detector background consists of foreground and background components. The foreground components include the instrumental dark current (which is negligible for both the UVOT and *GALEX*), instrumental scattered light (produced by off-axis light reflected from the detector housing and filter windows onto the chip), air-glow, zodiacal light (which is much more important in the near UV bands), and the Galactic cirrus. Although the contribution of cirrus decreases with increasing Galactic latitude, it is important at all latitudes. Finally, there is the extragalactic UV background that likely originates in galaxies.

The airglow, zodiacal light and amount of instrumen-

tal scattered light vary with the orbital position of the satellite and pointing direction, so the total on-field background varies between observations of a given object. This is most relevant for *Swift*, where we combine multiple exposures to create a final image. In the rest of this paper, we use the term “background” to refer to the sum of the foreground and background components including residual instrumental scattered light unless otherwise specified.

3.2. Diffuse Scattered Light Artifacts

Both *GALEX* and the UVOT have diffuse scattered light artifacts that can cover large portions of the chip. There are both persistent and transient artifacts, where persistent artifacts are those that are produced predictably under given circumstances.

The persistent artifacts include source-specific patterns that are most obvious around bright stars as well as filter-specific patterns in the UVOT that cover the entire chip. The most common source-specific patterns are out-of-focus ghost images that occur near the primary image and take the form of rings owing to the shape and geometry of the telescope mirrors (often called “smoke” or “halo” rings). These rings have a characteristic size and morphology based on the optics (in the UVOT, for example, the dimmer “halo rings” have an outer radius of 2 arcmin). The ghost images result from light that internally reflects in the detector window (Breeveld et al. 2010), so they actually occur around every source for which the ghost image falls onto the chip; whether a ring is visible depends on the source brightness. The filter patterns (Figure 2) affect every UVOT exposure and are produced by off-axis light that reflects onto the chip.

Transient artifacts are most commonly large streaks of scattered light across the chip, but some exposures also have a scattered light gradient that covers most of the chip. The brightnesses and widths of the streaks vary, and other artifacts may appear if there is a very bright source nearby but outside the field of view.

With *GALEX*, both persistent and transient artifacts are an issue because there are typically just a few deep exposures of a given target. *GALEX* counts events and reconstructs images based on knowledge of the spacecraft attitude, so in principle it is possible to filter the event

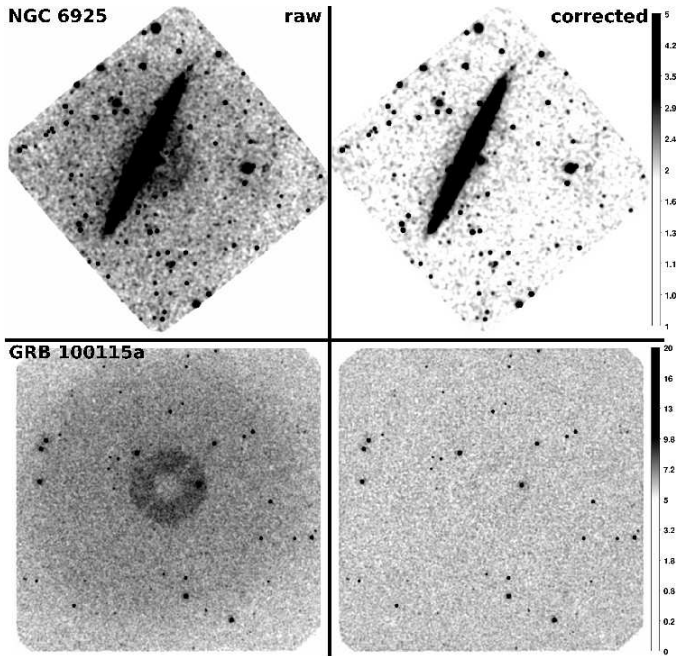


Figure 4. Raw and corrected ~ 1.5 ks images in two fields in the *uvw1* filter (where the central halo ring is a useful reference). The scale and color map are the same between raw and corrected images, and in each field we have clipped the scale at a low level to highlight the background.

list by time. However, the transient artifacts are dim (so they cannot be easily identified in a light curve) and have an unknown time dependence, so we discard exposures where the target galaxy is affected by large-scale transient artifacts. Only a few galaxies in the sample are near bright stars that produce smoke rings, and in these cases we simply mask the artifact.

Swift observations consist of many short exposures with small pointing offsets, so the persistent artifacts are more important than in *GALEX*. Thus, we developed a way to subtract the filter patterns. These patterns consist of a large disk of scattered light (the large feature that fills most of each panel in Figure 2) whose brightness declines radially outwards. The variation is significant, as is the absolute contribution to the background (up to 30%). In the *uvw1* and *uvw2* filters, these patterns include 2 arcmin halo rings that are fixed in position in chip coordinates. The *uvm2* filter does not appear to have halo rings, possibly because it is a narrower filter (for a more in-depth discussion of these patterns, see Breeveld et al. 2010). The patterns are produced by the optics, so if only a portion of the chip is exposed (a “windowed” image), that section receives the same part of the pattern it would if the entire chip were exposed. However, the pattern does shift slightly (a few pixels) between exposures in detector coordinates because the optical axis is not always centered on the chip center.

There is presently no correction in the UVOT calibration software for this artifact, so we created templates in each filter that we scale and subtract to leave a flat background. This is possible because the scattered light is always “extra” light that is a linear function of the true sky background and the patterns are fixed in detector coordinates. Assuming the true sky background is

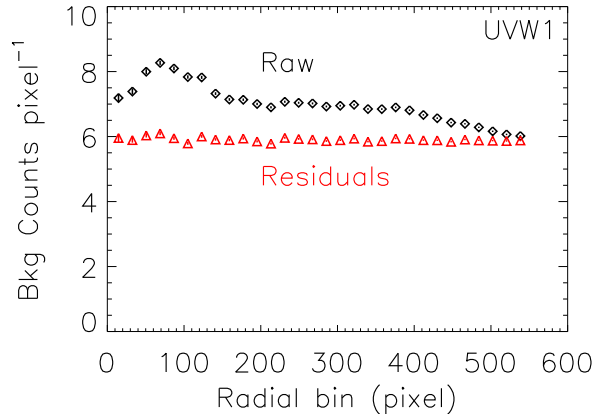


Figure 5. Radial profiles for the images shown in the bottom two panels of Figure 4 (GRB 100115a). We have subtracted point sources and measure the radial profile from the center of the halo ring (which is not perfectly centered on the chip). The error bars are smaller than the plot symbols. Cleaning removes over 95% of the scattered light.

flat across the field of view, the background in pixel i is

$$B_i = B_{\text{sky}} + mB_{\text{sky}}f(x_i, y_i) \quad (2)$$

where m is the scaling factor and $f(x_i, y_i)$ is the fixed normalized distribution of the filter pattern. The appropriateness of adopting m can be seen in Figure 3, which shows the dependence of the background-subtracted “surface brightness” in the brighter halo ring that is part of the filter pattern in the *uvw1* filter (Figure 2) on the sky background measured at the chip edges. The slopes are different in the other filters (probably because the feature we normalize to is different), but the relation remains linear.

The filter pattern $f(x, y)$ was generated in a similar way to the “blank sky” images in Figure 2. We used full-frame exposures of 1 ks or more in sparse fields with no bright sources, extended emission, or background gradients. The source exposures were chosen from the large number of gamma-ray burst follow-up observations in the archive. Each exposure was processed using the *Swift* pipeline up through flat-fielding, whereupon we masked all sources, subtracted the sky background measured at the mostly unaffected edges of the chip, and corrected for the large-scale sensitivity variations on the chip. The exposure-corrected images were stacked in detector coordinates, smoothed by a Gaussian kernel with $\sigma = 3$ pixels, and normalized.

We subtract the filter pattern after flat-fielding but before the transformation from detector to sky coordinates. The position of the template is first matched to the image binning and window, then we mask point sources and smooth a copy of the image. The “true” sky background is measured at the chip edges where the chip is fully exposed and the template surface brightness is less than 5% of its peak. Because of the scatter in the relationship between B_{sky} and m (e.g., Figure 3), we use least-squares fitting to minimize the residuals against what we assume to be a flat background. Since the background may not be perfectly flat, the flatness of the residuals is verified by binning the image by 16 pixels and measuring the variance and azimuthally averaged radial profile over

the fully exposed portion of the chip. When the results are not flat or the variance is high, we inspect the images visually and adjust the scaling factor (in such cases, the pattern or its inverse is typically visible in a smoothed image).

This method is demonstrated in the *uvw1* filter in Figure 4. The top two panels show the method as applied to a 1.4 ks exposure of NGC 6925 and the bottom two panels show a 1.6 ks exposure of a sparse field with no extended emission (GRB 10015a, obsID 20126003). For both objects, we have clipped the maximum pixel values to show the background more clearly and lightly smoothed the field, but the scaling and color map are the same between the images. In the gamma-ray burst field one can see the filter pattern very clearly along with the telescope struts in the center halo ring.

Subtraction typically accounts for more than 95% of the filter pattern light, making the residual smaller and more spatially uniform than other background sources. Figure 5 shows the azimuthally averaged radial profile for the two gamma-ray burst field images in Figure 4.

After subtracting the filter pattern, we transform to sky coordinates and proceed with the remainder of the UVOT pipeline to produce reduced, calibrated exposures. However, we must insert one more step into the pipeline because the UVOT pixel scale is slightly non-uniform (Breeveld et al. 2010), but during the sky transformation (using the UVOT tool SWIFTXFORM) the plate scale is made uniform in a way that conserves flux. In other words, a truly uniform sky background would *not* appear perfectly uniform in the raw image, but our template subtraction assumes that it is. Thus, we apply a distortion correction to account for this assumption analogous to SWIFTXFORM. The result is a flat background in the sky image.

Halo rings produced by bright stars are not removed in the pipeline process. The scatter in the relationship between the source count rate and the ring “surface brightness” is too high to make automatic removal reliable, especially for short exposures and dimmer sources. It is possible to detect and subtract these rings because they are anchored to their progenitor star, so we can use a ring template even for faint rings. However, if the star is within the halo detection zone, the residuals can have a large variance and it is better to mask the region or discard the exposure.

3.3. Residual Background Variability and σ_{sky}

The sensitivity in the *Swift* and *GALEX* data is limited by background spatial variation (photon counting noise can be reduced well below 1% of background by using deep exposures and averaging the flux over large bins).

Many *Swift* exposures have faint transient instrumental artifacts, such as broad, faint streaks parallel to a chip edge or background gradients. When these are bright enough to detect (which still requires smoothing and clipping the image), we discard the exposure, but often the artifacts are undetectable (when combining exposures, they are smoothed to some extent because of the different roll angles). Likewise, there are small variations in the astrophysical scattered light from the Galactic cirrus across many fields, so the “true” mean background light differs across the chip. These differences are generally

larger than the standard deviation measured in a small region of uniform background and dominate the uncertainty in our flux measurements.

To characterize the uncertainty, we measure the variance in the background count rate measured in many regions across the fully exposed portion of the chip. For *GALEX* we restrict the region of interest to the *Swift* UVOT field of view for consistency. The background fields are then defined in the UVOT images using source-free regions more than 2 arcmin away from sources whose count rates might produce a bright halo ring (typically we use a cutoff of a total count rate less than 50 counts s^{-1}). The scattered light background count rate appears to follow a Poisson distribution when examining “event”-mode data and the number of background counts is quite high, so we adopt the standard deviation of the background σ_{sky} as our estimate for the uncertainty in background subtraction. For most of the galaxies in our sample, $\sigma_{sky} \sim 0.1 - 4\%$ of the mean sky background.

3.4. Stellar Halo Rings

In both *Swift* and *GALEX* a small fraction of the incident photons from a given source are scattered by the optics into a region around the source, producing ghost images with an instrument-specific pattern as described above. For example, in the UVOT, which produces visible ghost images for fainter stars than *GALEX*, the characteristic outer radius of the larger ghost images (the “halo rings”) is 2 arcmin. The rings are only visible for the brightest sources, but dimmer sources still scatter incident flux; they simply do not fill in the pattern. We denote this scattered light F_{ring} . This behavior can be generalized to extended sources such as galaxies, where the total instrumental scattered light F_{scat} is the sum of F_{ring} over all the sources in the galaxy.

Considering the angular sizes of galaxy halos, the contribution of F_{scat} to halo light may be important. However, the dependence of F_{ring} on the count rate of the associated star, F_{star} , is unknown. Because of the faintness of the rings it is also not clear whether F_{ring} is a continuous function of F_{star} or of there is a threshold F_{star} below which reflected light is not transmitted to the chip.

In this subsection, we examine the dependence of F_{ring} on F_{star} at low count rates to assess what F_{scat} we might expect from the galaxies in our sample. These galaxies have total count rates between $1 - 200 \text{ counts s}^{-1}$, but the compact clumps that characterize the emission typically have count rates of $1 - 10 \times 10^{-4} \text{ counts s}^{-1}$. Clearly, F_{ring} must be less than this, but if it is not much less then F_{scat} will be a significant fraction of the background.

To address this issue we measured F_{ring} around a sample of stars from the *Swift* gamma-ray burst observations between 2008–2013, which randomly sample the sky. We only included exposures greater than 800 s for good background statistics and rejected exposures with strong background variation. The data were processed in an analogous way to the analysis sample.

For stars with visible halo rings we measured the background-subtracted count rate. Stars without immediately apparent halo rings may still have *detectable* halo rings, but there are two challenges. First, halo rings have large offsets from the primary images when the source has a large offset from the optical axis, so we restricted our

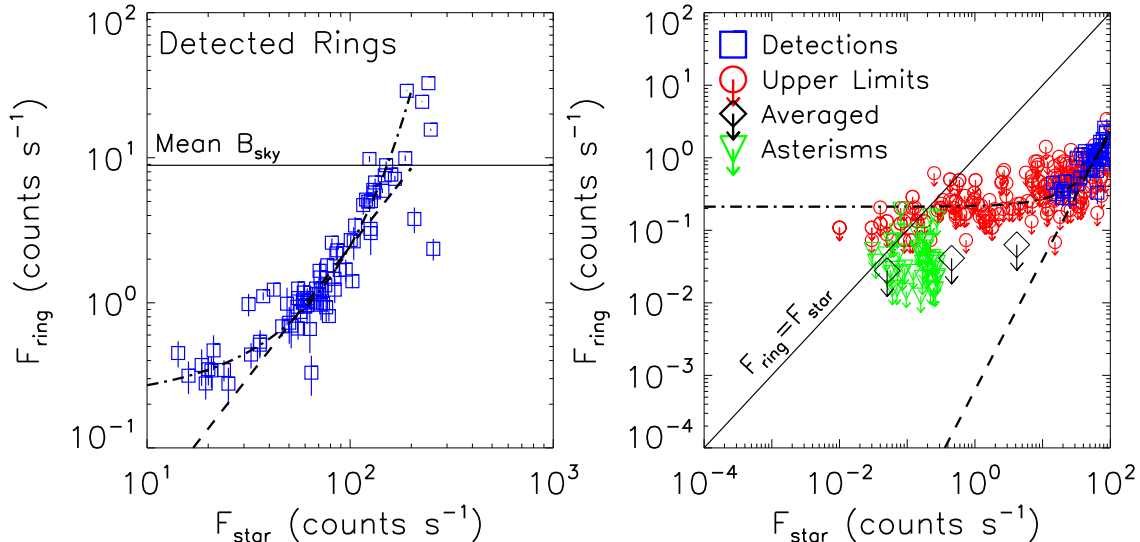


Figure 6. *Left:* Instrumental scattered light flux (F_{ring}) as a function of the incident flux of the associated star (F_{star}) for the *Swift wvm2* filter. The best exponential and log-linear models have been overplotted. *Right:* F_{ring} detections and limits at lower F_{star} , including limits from averaged data. See Section 3 for discussion.

sample to sources within 3–4 arcmin of the chip center where this is not a significant issue. Unfortunately, the *wvm1* and *wvm2* filter patterns have bright halo ring features near the chip center (Figure 2), so we restrict the analysis to the *wvm2* filter. Second, if there is no visible halo ring we require the star to be by far the brightest in its vicinity so we do not measure competing halo rings. We then measure F_{ring} within the 2 arcmin around the star while also avoiding the primary image of the star and any other nearby sources to 95% of the encircled energy in the point-spread function. The values are scaled by the area in a complete ring. We measured F_{ring} for all stars above $F_{\text{star}} = 10 \text{ counts s}^{-1}$ that meet these criteria. The sample was extended to $F_{\text{star}} > 0.01 \text{ counts s}^{-1}$, but isolated stars are less common, and we limited the lower flux sample to fields with lower, more uniform backgrounds.

Halo rings are only detected above $F_{\text{star}} = 10 \text{ counts s}^{-1}$. The detections are shown in the left panel of Figure 6. Nondetections are omitted for clarity, but are shown in the right panel. Above $F_{\text{star}} \sim 130 \text{ counts s}^{-1}$ the scatter increases markedly for unknown reasons. One possibility is that we see a secondary ring. Very bright stars sometimes produce multiple halo rings, where one is much brighter than the others. If a bright star’s primary ring fell off the chip but its secondary did not, we might mistake the secondary ring for the primary. In any case, as a first step to determine the dependence of F_{ring} on F_{star} we fit the detected F_{ring} values below $F_{\text{star}} = 130 \text{ counts s}^{-1}$ with simple models. The scatter precludes formally good fits for any model we tried (linear, log-linear, quadratic, and exponential), but the exponential model is the best fit. The best exponential and linear models are overlaid in Figure 6, where it is clear that the exponential model does a better job at reproducing the curvature in the data.

However, it is clear from the right panel of Figure 6 that the exponential model becomes unphysical for stars with $F_{\text{star}} \lesssim 0.2 \text{ counts s}^{-1}$ and is also disfavored by the upper limits we have measured. The constraints pro-

vided by individual stars are limited by the *Swift* background, so we averaged over the F_{ring} measurements below $F_{\text{star}} = 10 \text{ counts s}^{-1}$, grouping stars in each decadal bin. After averaging there were still no detections, but the upper limits were reduced (diamonds in Figure 6).

Significantly tightening the constraints would require a much larger sample, but at low count rates another way of averaging is to use small asterisms. We measured F_{ring} in the region around isolated groups of dim stars, where the asterisms comprise 3–15 members contained within 1 arcmin in the inner portion of the chip. Since these stars should produce overlapping halo rings, we measured the average F_{ring} per star and the mean count rate F_{star} . Again, there are no detections, but the upper limits (shown as inverted triangles in Figure 6) improve the constraint on F_{ring} at low count rates.

The functional form of F_{ring} below $F_{\text{star}} \sim 10 \text{ counts s}^{-1}$ cannot be determined, but we can make some inferences from the limits and the requirement that $F_{\text{ring}} < F_{\text{star}}$ (Figure 6). The linear fit to detected rings suggests a ratio of $F_{\text{ring}}/F_{\text{star}} \lesssim 0.01$, while the cluster of detected rings at $F_{\text{star}} \sim 10 \text{ counts s}^{-1}$ is consistent with a ratio of 0.02–0.04. The averaged limit between $F_{\text{star}} = 1 - 10 \text{ counts s}^{-1}$ rules out a significantly larger value. At lower count rates, the limits only constrain the ratio to be $F_{\text{ring}}/F_{\text{star}} < 0.1$.

The total instrumental scattered light we expect from the galaxy is between $F_{\text{scat}} = 0.01 - 0.1 F_{\text{gal}}$. For $F_{\text{gal}} = 200 \text{ counts s}^{-1}$ (at the high end of our sample), we would expect F_{scat} between 2–20 counts s^{-1} . However, galaxies with higher fluxes tend to be closer, and the angular size of the galaxy is important because a given clump in the galaxy only contaminates the surrounding 2 arcmin with instrumental scattered light. For a galaxy larger than 2 arcmin, only some of the scattered light contaminates the halo (the rest is coincident on the chip with the galaxy itself), and the exact contribution at any point in the halo depends on the re-

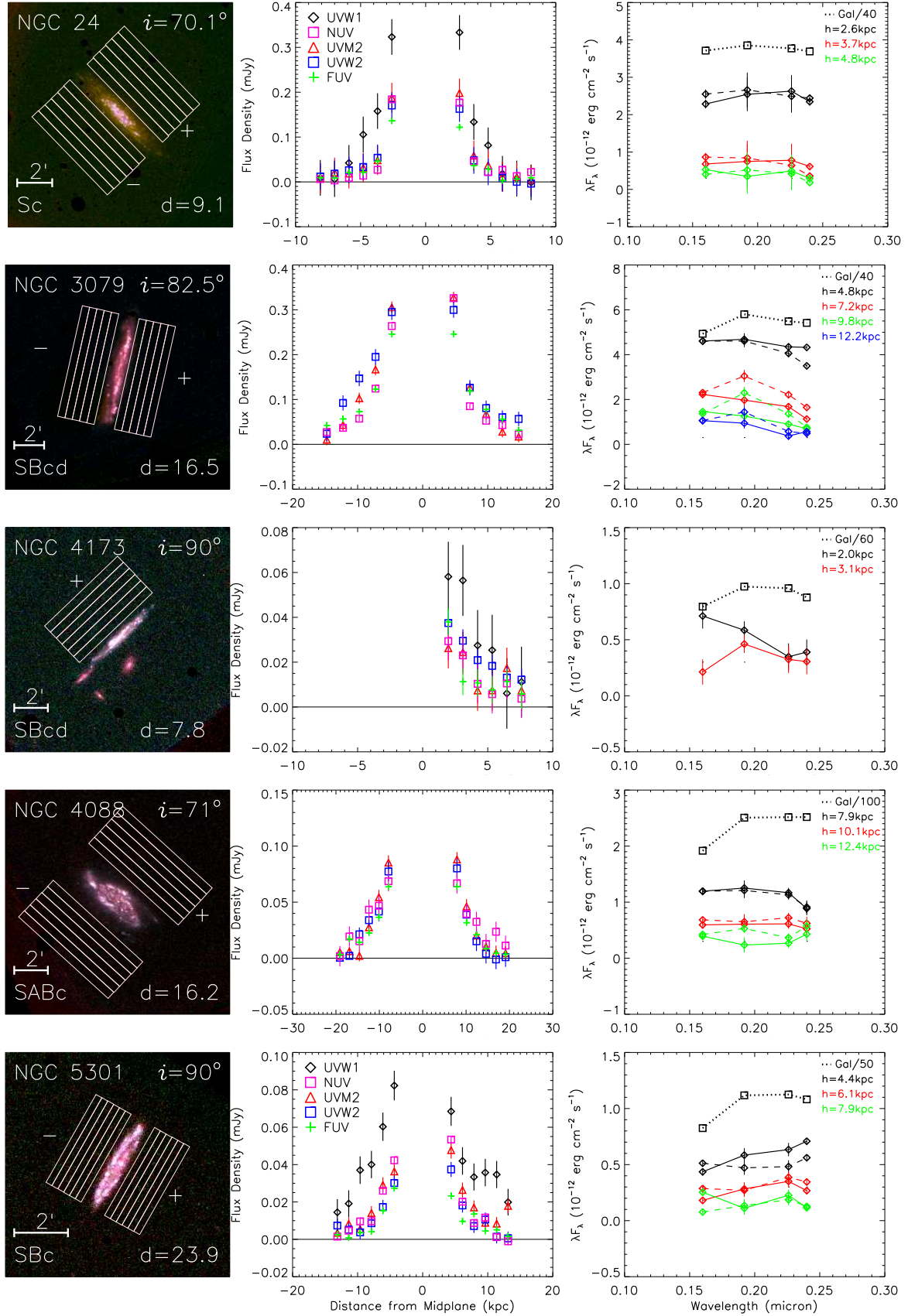


Figure 7. Halo emission fluxes and SEDs for Sc through Sd morphology galaxies in our sample. *Left panels:* RGB image made from the *uvw1*, *uvw2*, and *uvw2* images, annotated with the galaxy name, inclination, morphological type, and distance in Mpc from Table 2. Flux extraction bins are overlaid in white, and extragalactic point sources have been masked. *Central panels:* F_ν as a function of height above the midplane in each of the UV bands (*uvw1*: black diamonds, NUV: pink squares, *uvw2*: red triangles, *uvw2*: blue squares, and FUV: green crosses). *Right panels:* 4-point SED as a function of height above the midplane using (from left to right) the FUV, *uvw2*, *uvw2*, and NUV fluxes. The SEDs are colored as a function of height, and solid/dashed lines at each height represent the fluxes on the “positive” and “negative” sides of the midplane respectively.

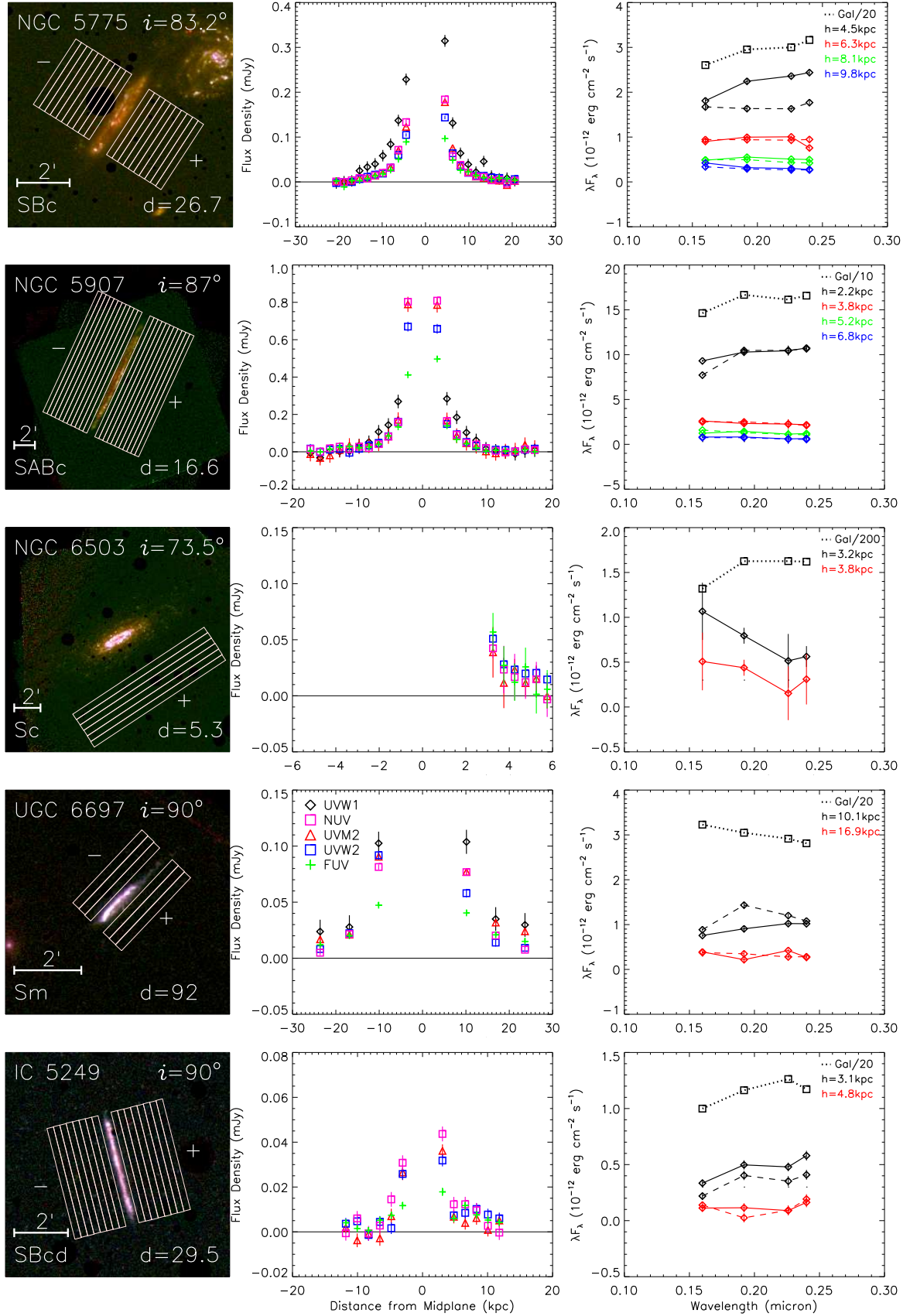


Figure 7. Halo emission fluxes and SEDs for Scd spiral galaxies in our sample *continued*.

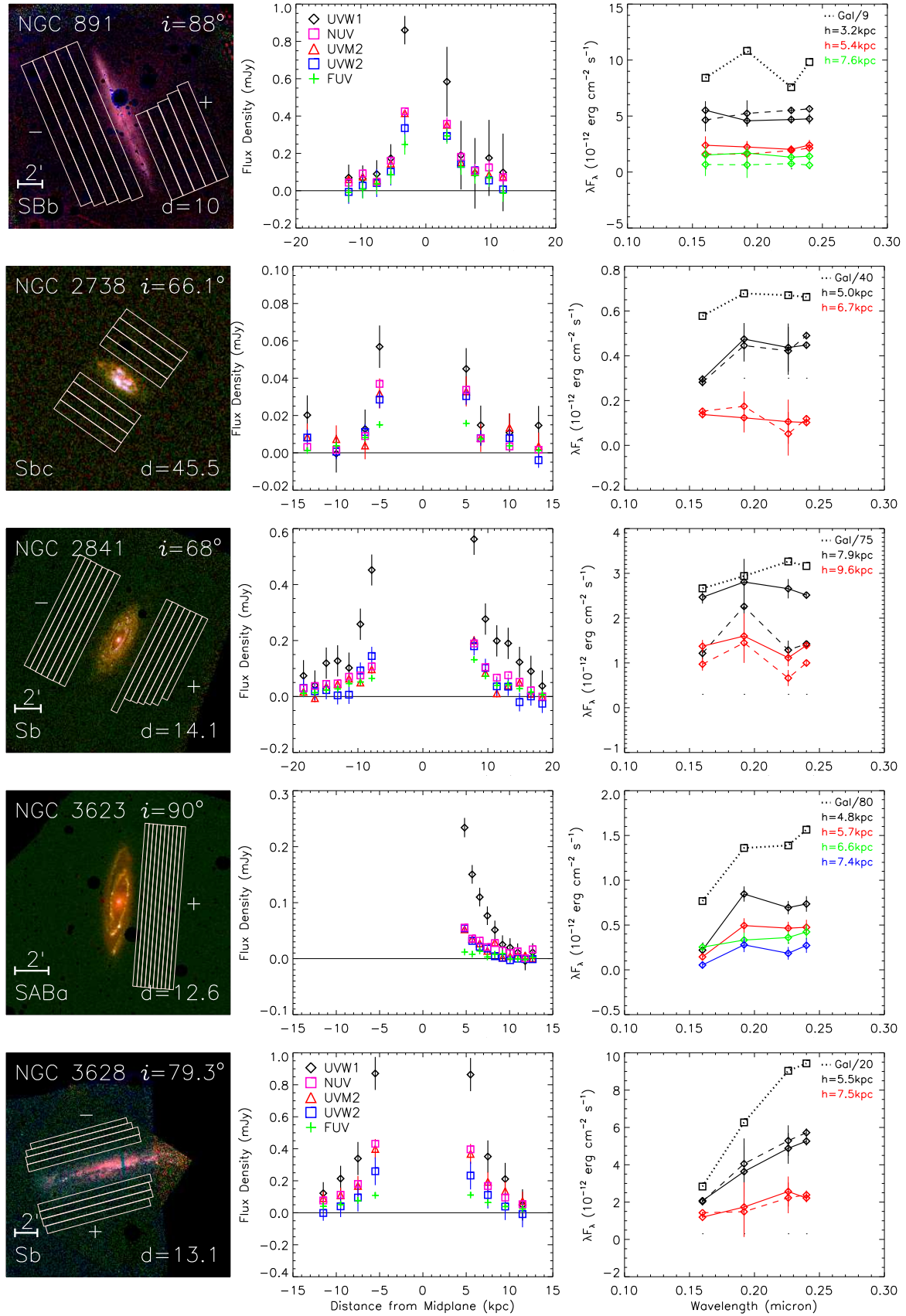


Figure 8. Halo emission fluxes and SEDs for Sa through Sbc morphology galaxies in our sample. The plot format and symbols are the same as in Figure 7.

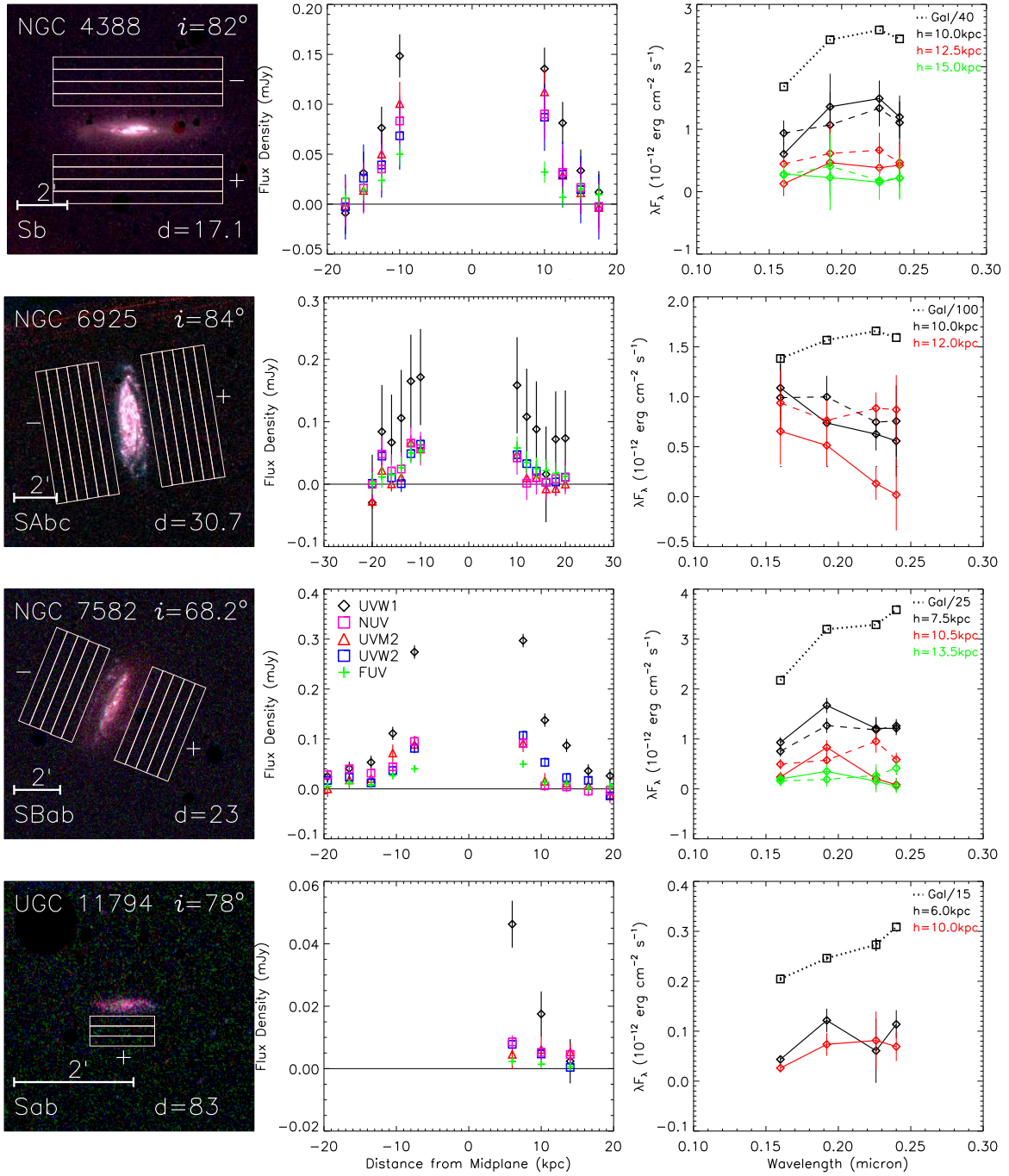


Figure 8. Halo emission fluxes and SEDs for Sa through Sbc morphology galaxies in our sample *continued*.

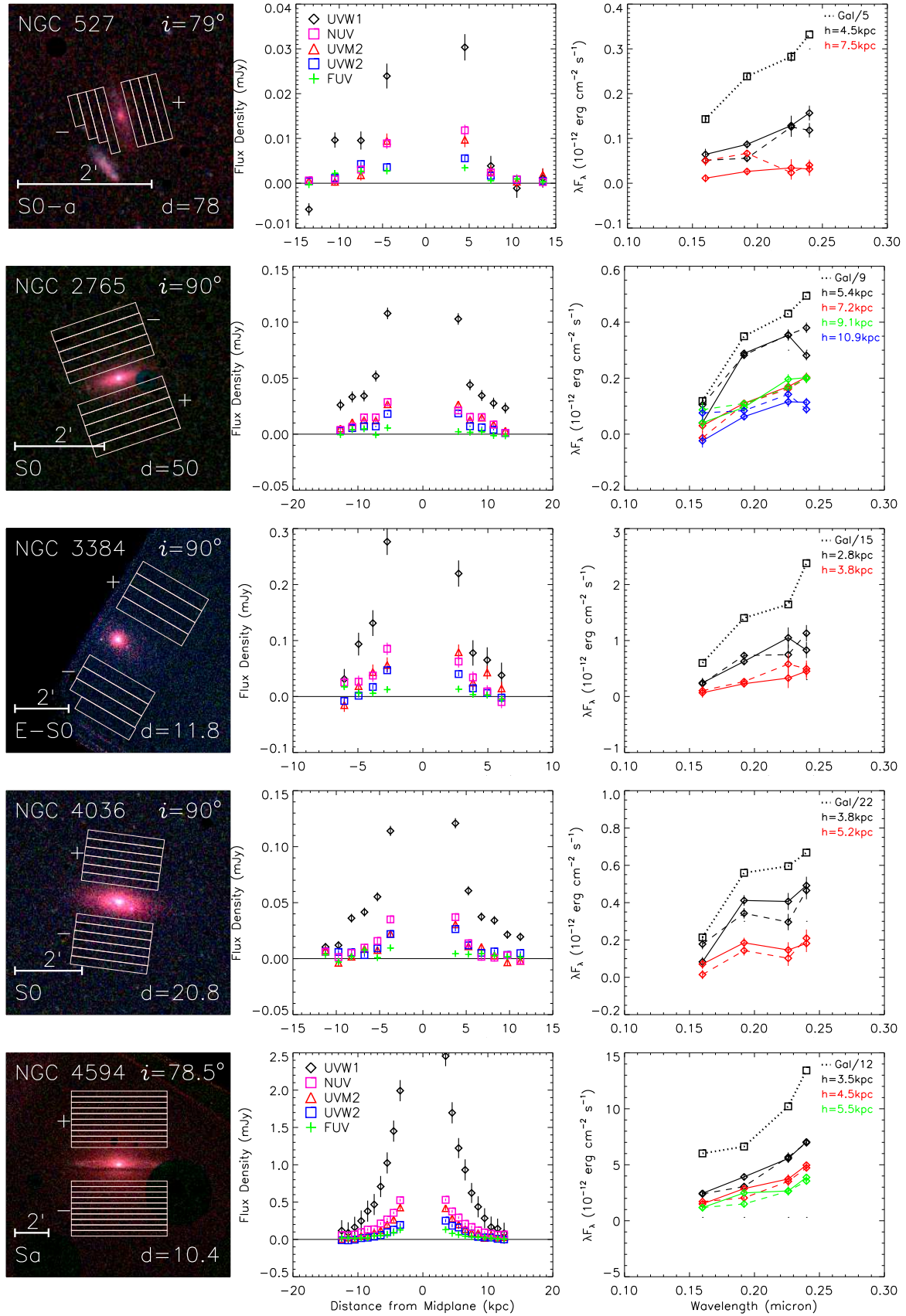


Figure 9. Halo emission fluxes and SEDs for highly inclined S0 galaxies in our sample (NGC 4594 is also included). The plot format and symbols are the same as in Figure 7.

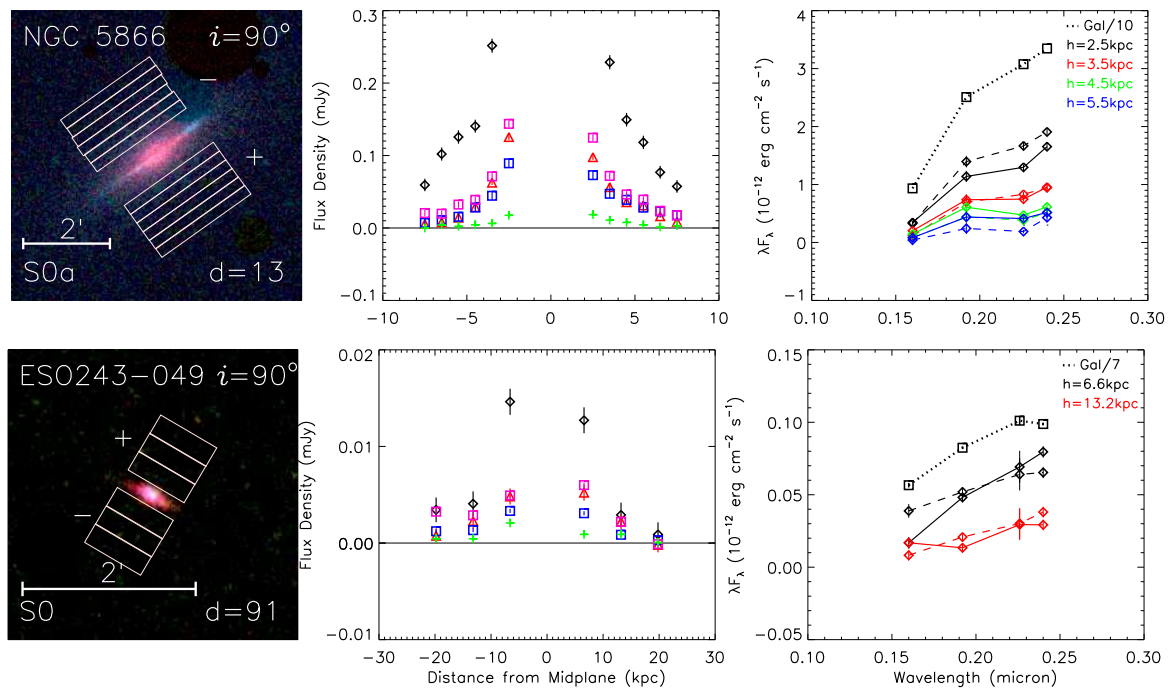


Figure 9. Halo emission fluxes and SEDs for highly inclined S0 galaxies in our sample *continued*

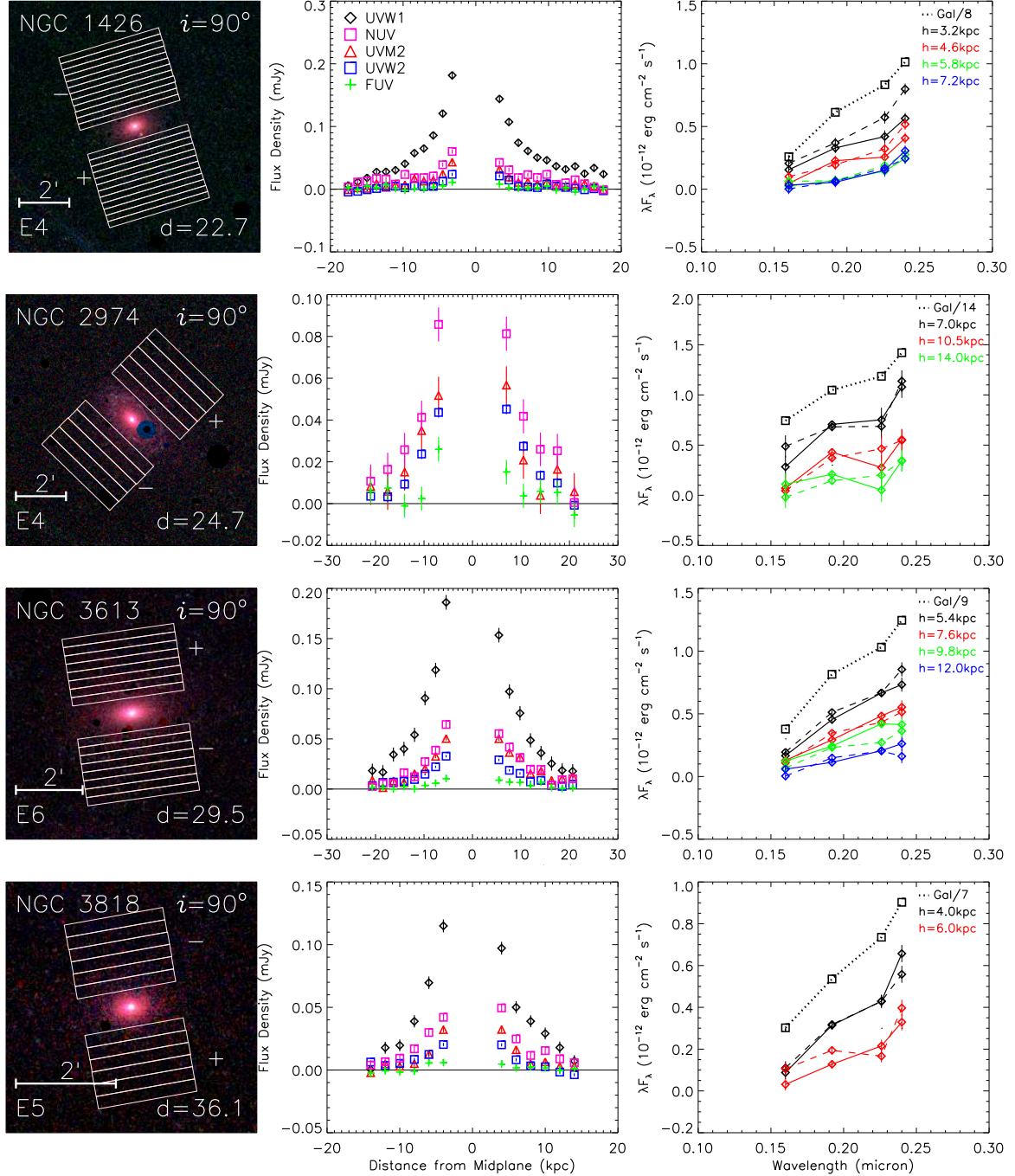


Figure 10. Halo emission fluxes and SEDs for elongated elliptical galaxies in our sample. The plot format and symbols are the same as in Figure 7.

gion of the galaxy within 2 arcmin of that point on the chip. In our sample, we find that the galaxy count rates that could contribute to instrumental scattered light in the halo are $0.1\text{--}50\text{ counts s}^{-1}$, with higher count rates nearer the galaxy. In the “worst case scenario” (bright galaxy, relatively compact, measurements near the disk), we expect $F_{\text{scat}} \sim 0.1 B_{\text{sky}}$, whereas at the low end we expect $F_{\text{scat}} < 0.001 B_{\text{sky}}$. This is a wide range, but (based on count rates, angular sizes, and Figure 6), we suppose that F_{scat} is 1% or less of B_{sky} for most of our sample.

The typical σ_{sky} is 0.1–4% of B_{sky} .

4. RESULTS

We measured halo fluxes above the midplanes of the galaxies in our sample from the reduced, cleaned images in each filter. The results are shown in Figures 7, 8, 9, and 10 which show, respectively, spiral galaxies of type Sc through Sd, spiral galaxies of type Sab through Sbc, S0 galaxies, and elliptical galaxies. For our purposes, we put the Sa galaxy NGC 4594 (M104) in the S0 category

Table 4
Integrated UV Fluxes of Halos and Galaxies

Galaxy	$uvw1$ (mJy)	NUV (mJy)	Halo Flux $wm2$ (mJy)	$uvw2$ (mJy)	FUV (mJy)	$uvw1$ (mJy)	NUV (mJy)	Galaxy Flux $wm2$ (mJy)	$uvw2$ (mJy)	FUV (mJy)	$uvw2$ Corr
ESO 243-049	0.039±0.003	0.019±0.001	0.015±0.002	0.010±0.001	0.005±0.001	0.175±0.002	0.052±0.001	0.053±0.002	0.037±0.001	0.021±0.001	0.65
IC 5249	0.25±0.02	0.13±0.01	0.09±0.01	0.110±0.009	0.084±0.006	2.37±0.01	1.78±0.01	1.9±0.01	1.49±0.01	1.06±0.01	0.93
NGC 24	1.220±0.014	0.55±0.01	0.6±0.1	0.55±0.09	0.45±0.02	14.3±0.05	11.1±0.02	11.3±0.04	9.86±0.04	7.92±0.03	0.93
NGC 527	0.072±0.006	0.028±0.001	0.027±0.003	0.018±0.001	0.013±0.001	0.43±0.01	0.125±0.002	0.105±0.003	0.076±0.002	0.037±0.002	0.65
NGC 891	2.4±0.5	1.6±0.1	1.52±0.07	1.1±0.2	0.9±0.1	13.0±0.1	6.5±0.1	5.2±0.1	6.21±0.05	4.13±0.05	0.93
NGC 1426	1.34±0.02	0.45±0.02	0.26±0.02	0.11±0.01	0.06±0.01	1.91±0.01	0.612±0.005	0.502±0.005	0.314±0.005	0.11±0.004	0.60
NGC 2738	0.17±0.03	0.097±0.003	0.11±0.02	0.09±0.01	0.056±0.002	2.94±0.05	2.00±0.01	2.02±0.04	1.84±0.02	1.233±0.007	0.93
NGC 2765	0.49±0.02	0.131±0.004	0.133±0.004	0.077±0.003	0.016±0.004	1.01±0.01	0.335±0.003	0.292±0.002	0.205±0.003	0.057±0.004	0.65
NGC 2841	2.6±0.2	0.92±0.03	0.69±0.01	0.3±0.1	0.58±0.03	35.6±0.1	17.87±0.03	18.4±0.05	14.11±0.06	10.65±0.02	0.93
NGC 2974	-	0.35±0.03	0.22±0.03	0.18±0.01	0.07±0.02	-	1.53±0.01	1.25±0.01	0.939±0.005	0.555±0.008	0.60
NGC 3079	-	1.04±0.02	1.19±0.04	1.38±0.05	1.07±0.01	-	16.32±0.01	16.53±0.02	14.87±0.04	10.52±0.01	0.93
NGC 3384	0.93±0.06	0.27±0.03	0.26±0.04	0.12±0.02	0.055±0.01	7.56±0.04	2.69±0.01	1.47±0.04	1.35±0.03	0.48±0.01	0.65
NGC 3613	1.03±0.03	0.36±0.02	0.327±0.007	0.194±0.008	0.060±0.005	2.85±0.01	0.845±0.006	0.699±0.003	0.471±0.003	0.181±0.004	0.60
NGC 3623	0.69±0.05	0.23±0.02	0.18±0.02	0.13±0.02	0.052±0.006	22.2±0.2	9.45±0.07	8.36±0.06	7.05±0.06	3.27±0.03	0.85
NGC 3628	3.0±0.3	1.51±0.04	1.53±0.2	0.8±0.2	0.511±0.007	33.0±0.1	14.21±0.02	14.0±0.1	8.03±0.05	3.02±0.01	0.93
NGC 3818	0.50±0.02	0.22±0.01	0.122±0.008	0.085±0.005	0.017±0.005	1.44±0.01	0.48±0.01	0.074±0.004	0.242±0.003	0.113±0.004	0.60
NGC 4036	0.56±0.01	0.13±0.01	0.09±0.01	0.11±0.01	0.038±0.004	4.85±0.02	1.11±0.01	0.99±0.01	0.792±0.003	0.25±0.04	0.65
NGC 4088	-	0.38±0.03	0.35±0.02	0.31±0.03	0.29±0.01	-	18.97±0.02	18.96±0.01	16.05±0.02	10.28±0.02	0.93
NGC 4173	0.18±0.04	0.083±0.02	0.09±0.02	0.13±0.01	0.08±0.01	5.06±0.02	3.97±0.01	4.34±0.02	3.89±0.01	2.55±0.02	0.93
NGC 4388	0.50±0.06	0.27±0.07	0.31±0.06	0.26±0.09	0.16±0.03	11.07±0.06	4.70±0.02	5.04±0.01	4.16±0.01	3.35±0.02	0.93
NGC 4594	14.7±0.6	3.88±0.08	2.6±0.1	1.41±0.09	0.90±0.04	40.8±0.2	12.14±0.02	9.2±0.1	5.1±0.1	3.84±0.02	0.65
NGC 5301	0.49±0.03	0.19±0.01	0.22±0.01	0.15±0.01	0.111±0.004	6.28±0.03	4.08±0.01	4.26±0.03	3.54±0.02	2.22±0.01	0.93
NGC 5775	1.4±0.06	0.62±0.02	0.623±0.009	0.56±0.02	0.445±0.008	8.21±0.02	4.77±0.01	4.52±0.01	3.78±0.01	2.78±0.01	0.93
NGC 5866	2.1±0.03	0.65±0.01	0.49±0.01	0.42±0.02	0.080±0.003	8.96±0.03	2.52±0.01	2.32±0.02	1.61±0.01	0.498±0.006	0.65
NGC 5907	3.5±0.2	2.40±0.08	2.3±0.2	2.1±0.1	1.59±0.02	18.67±0.03	12.45±0.02	12.16±0.05	10.78±0.04	7.84±0.02	0.93
NGC 6503	0.2±0.1	0.11±0.04	0.10±0.04	0.16±0.01	0.13±0.04	33.66±0.07	24.43±0.02	24.50±0.02	20.81±0.02	14.08±0.03	0.93
NGC 6925	1.1±0.3	0.29±0.09	0.18±0.04	0.28±0.05	0.33±0.06	17.63±0.09	11.97±0.02	12.50±0.02	9.71±0.02	7.38±0.03	0.93
NGC 7090	-	-	1.65±0.09	1.40±0.05	-	-	-	11.05±0.02	9.49±0.02	-	0.93
NGC 7582	1.09±0.04	0.33±0.03	0.31±0.05	0.36±0.04	0.17±0.02	12.27±0.03	6.76±0.02	6.19±0.06	5.11±0.04	2.92±0.01	0.85
UGC 6697	0.32±0.02	0.212±0.005	0.261±0.006	0.203±0.008	0.155±0.004	4.65±0.03	4.23±0.01	4.39±0.02	3.90±0.01	3.44±0.01	0.93
UGC 11794	0.07±0.01	0.018±0.004	0.016±0.007	0.012±0.004	0.004±0.001	0.65±0.01	0.349±0.003	0.33±0.01	0.26±0.01	0.164±0.003	0.85

Note. — We report the total halo flux measured in each filter by summing over the extraction bins shown in Figures 7, 8, 9, and 10. The galaxy flux is measured in a region roughly spanning the space between the boxes, but the region is defined by SExtractor. The error bar is dominated by uncertainty in the background. The $uvw2$ fluxes are corrected as described in the text, but the $uvw1$ fluxes are not.

because of its giant stellar halo and bulge; as we shall see, its spectral characteristics agree with this categorization.

There are three panels per galaxy in these figures. The left panel is a false-color image made from the *uvw1*, *uvm2*, and *uvw2* filters with point sources outside the galaxy subtracted. The white boxes indicate the flux measurement boxes used for the central panel, which shows the flux density at a projected height z in kpc based on the distance adopted for each galaxy (Table 2). We do *not* correct the distances by $\sin i$ because in some cases the inclination angle is suspect, but for the less inclined galaxies most halo emission comes from regions closer to the galaxy than the nominal projected distances. The inclinations in the early-type galaxies refer to the projected elongation.

Extended diffuse UV emission is detected around each galaxy in our sample, with a maximum extent of 5–20 kpc from the midplane. The flux profiles appear to decline exponentially, with some asymmetry across the midplane or profiles that differ between filters. The halo fluxes range from 2–50% of the background in bins with 3σ detections.

The right-hand panel gives an orthogonal view of these fluxes by showing a four-point UV SED as a function of z on both sides of the midplane (the solid and dashed lines of the same color). We also plot the SED of the galaxy, arbitrarily scaled to fit on the plot, as a dotted line. The upper right-hand corner of the panel shows the scaling factor and the heights of the halo SEDs. We show the NUV point with an artificial offset in wavelength for clarity (it is nominally calibrated to about the same wavelength as the *uvm2* filter but covers most of the same *uvw1* region of the spectrum; see Figure 1). The *uvw1* flux is not included in the SEDs because the red tail can easily put the effective wavelength close to the optical band.

In the remainder of this section, we describe the flux measurement, discuss the basic properties of the halo emission, and compare the different types of galaxies.

4.1. Flux Measurements

Fluxes are computed from the background-subtracted count rates in the extraction boxes shown in the galaxy image panels. The total halo fluxes in each filter are given in Table 4.

We sum the count rate in each box and scale it to a uniform box size (accounting for point source masks and non-uniform box sizes). In most cases, the correction is small (1–10%), but in some bins can exceed 50% because of bright stars or chip edges. The reported fluxes in such cases may be slightly too high or low, but for most galaxies this is not an issue. The location of the innermost box for each galaxy was chosen to be clearly above the disk for late-type galaxies and outside a few scale heights for E/S0 galaxies, but we do not use a uniform definition because of the different types and inclinations. Nonetheless, the boxes are defined conservatively to be at least a few kpc (projected) above the midplane, outside of several optical scale heights as seen around an edge-on system. We then subtract a mean background from the count rates and convert them to flux density using the conversion factors in Table 1, and correct for Galactic extinction using the Schlegel et al. (1998) dust map using the calibrations in Wyder et al. (2007) and

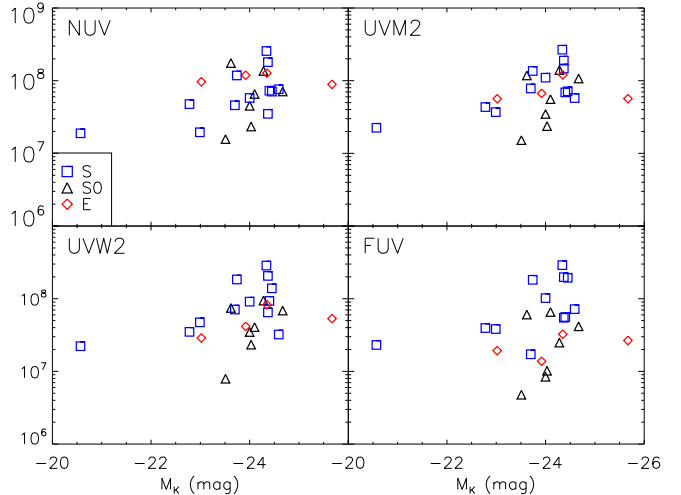


Figure 11. UV halo luminosities in each filter as a function of the absolute K -band magnitude M_K for spiral (blue squares), S0 (black triangles), and elliptical (red diamonds) galaxies. L_ν was computed in each filter based on the distance and magnitudes in Table 2 and UV fluxes in Table 4. See text for discussion.

Roming et al. (2009).

Finally, we apply the correction for the red leak in the *uvw2* filter as described above. As the true correction depends on the true spectrum, we report both the corrected flux and the correction factor in Table 4. The *uvw1* fluxes are not corrected and are not included in the SED plots (but we return to these in Section 7).

In Section 3 we argued that the contribution of instrumental scattered light from the galaxy to the measured light in the halo is typically a few percent of the background. Given the agreement between the *GALEX* and *Swift* flux profiles in the bright late-type galaxies (e.g., Figure 7) and the different systematic effects in each instrument, we posit that the contamination from instrumental scattered light is no worse than the error on the background σ_{sky} , which is dominated by spatial variation in the background.

4.2. Properties of the Halo Emission

From our flux measurements we can obtain three physical quantities: the luminosity, extent, and the SED of the halo emission. With the deeper data sets, we can map these quantities around the galaxy.

4.2.1. Luminosity

The luminosity $L_\nu = 4\pi d^2 F_\nu$ is computed from the integrated halo fluxes (Table 4). As most of the flux comes from near the galaxy, the true halo UV luminosity is sensitive to the choice of the innermost bin height; our L_ν values are measured starting a few kpc from the midplane (well above the optical disk).

Figure 11 shows L_ν as a function of M_K (galaxies with $M_K > -22$ mag are not shown). The different symbols break the galaxies up by type: blue squares represent late-type (Sab through Sd) galaxies, black triangles are S0 galaxies, and red diamonds are elliptical galaxies.

Most of the galaxies in the sample have M_K similar to the Milky Way ($M_K \sim -24$ mag) and are not cleanly separable in any of the bands. The largest differences are seen in the FUV band, where the elliptical and S0 galax-

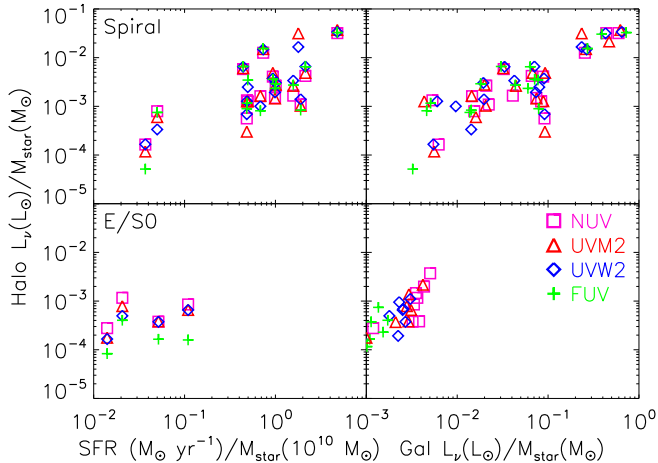


Figure 12. Specific halo luminosity in the NUV, *uvm2*, *uvw2*, and FUV bands plotted against specific SFR (left panels) and specific galaxy luminosity (right panels) for spiral and early-type galaxies (top and bottom panels). The values are divided by the stellar mass shown in Table 2. See text for discussion.

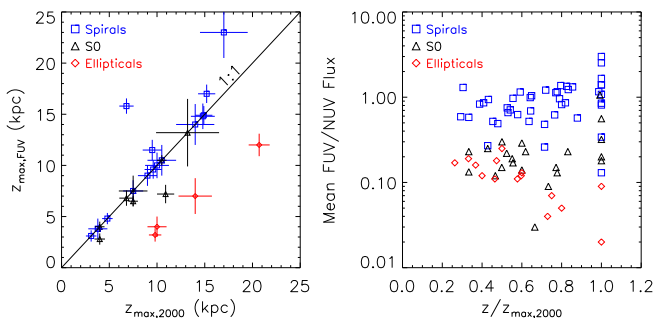


Figure 13. *Left:* A plot of the maximum extent (z_{max}) of the halo as measured in the FUV filter against the average z_{max} in the NUV, *uvm2*, and *uvw2* filters $z_{\text{max},2000}$ (see Section 4). The “error bars” are the width of the flux extraction bin representing z_{max} for each galaxy. *Right:* The ratio of the FUV to NUV fluxes as a function of height above the midplane for the galaxies in our sample, broken into spirals, S0s, and ellipticals. Error bars are omitted for clarity. See Section 4 for discussion.

ies tend to have lower FUV luminosities than the late-type galaxies; as we discuss below, this is even more apparent when comparing the fluxes as a function of height above the midplane. Since the galaxies have different sizes and the sample is not objectively defined, the overlap is not surprising.

In Figure 12 we show the specific integrated halo luminosities in the NUV (pink boxes), *uvm2* (red triangles), *uvw2* (blue diamonds), and FUV (green crosses) as a function of the specific SFR and the specific galactic luminosities, where “specific” is in reference to the stellar mass M_{star} (galaxies without the information to compute the SFR or M_{star} are omitted). We have separated the galaxies by type into spiral and early-type (E/S0) systems. To measure the correlation between these quantities (in each band), we use the Spearman ranked correlation coefficient ρ , which we prefer over the Pearson coefficient because of the small number of data points.

With regard to the SFR, the only significant correlation at better than 99% is in the *uvw2* band ($\rho = 0.67$,

$p = 0.004$). The other bands do not even have marginally significant correlations ($p = 0.16, 0.05$, and 0.24 for the NUV, *uvm2*, and FUV respectively). If we consider only specific $\text{SFR} > 0.1 M_\odot \text{ yr}^{-1}$, there is no significant correlation in any band, so among galaxies with SFR similar to or greater than the Milky Way the specific SFR does not predict the halo luminosity. For the early-type galaxies, there are not enough data to measure a significant correlation.

On the other hand, the specific halo luminosity in each band except the NUV is strongly and significantly correlated with the specific galaxy luminosity. For the NUV filter $\rho = 0.57$ and $p = 0.02$, for *uvm2* $\rho = 0.69$ and $p = 0.002$, for *uvw2* $\rho = 0.76$ and $p = 0.0004$, and for FUV $\rho = 0.80$ and $p = 0.0002$. For the early-type galaxies, what looks like a significant correlation in Figure 12 is due to offsets between each band (which also appear in the SEDs; cf. Figure 10), and the only significant correlation is in the FUV ($\rho = 0.86$ and $p = 0.007$). The others have $p > 0.05$.

We also measured the correlation between the halo luminosity and M_K and find no significant dependence in any band for the late-type galaxies, whereas for the early-type galaxies there is a significant correlation in the FUV ($\rho = 0.86$, $p = 0.0003$) and a marginally significant correlation in the NUV ($\rho = 0.59$, $p = 0.02$).

The correlation between halo and galaxy UV luminosity hints at a physical connection in the late-type galaxies, but the connection is evidently not mediated by rapid (present-day) star formation. The actual correlations may be even stronger, as we have made no attempt to correct for the effects of inclination and extinction.

4.2.2. Scale Heights and Maximum Extent of the Halo Emission

Differences between galaxy types are more evident when considering the UV luminosity as a function of height above the midplane $L_\nu(z)$. We cannot reliably measure scale heights for the halo emission in most galaxies because of the coarseness of the flux measurement bins and the differences in the bin widths between galaxies. For many galaxies, there is a large artificial minimum on the measurable scale height.

It is possible to measure a scale height in the galaxies with the best data (where the S/N is high in narrow bins). These include the late-type galaxies NGC 5775, NGC 5907, and NGC 3079, and the early-type galaxies NGC 4594, NGC 5866, and NGC 3613. We fit profiles of the form $I(z) = I_0 e^{-z/H}$ in each band for these galaxies, where we averaged the flux on each side of the midplane at each height, and the results are given in Table 5. The early-type galaxies are fit well in each band except the FUV by the exponential fit (we also tried Gaussian fits, which were never better for any galaxy), with best-fit scale heights of $H \sim 2.75 - 3.5$ kpc for NGC 4594, $H \sim 2 - 3$ kpc for NGC 5866, and $H \sim 6 - 8$ kpc for NGC 3613. The late-type galaxies also had generally good fits, although the exponential fit is too steep for most bands. We find $H \sim 2.5 - 3.5$ kpc for NGC 5775, $H \sim 2 - 3$ kpc for NGC 5907, and $H \sim 3 - 5$ kpc in NGC 3079.

The UV scale heights for the late-type galaxies are larger than the scale height of the thick disks, which range from 0.3–1.5 kpc (e.g., Yoachim & Dalcanton

Table 5
UV Scale Heights

Galaxy	H_{NUV} (kpc)	χ^2	H_{UVM2} (kpc)	χ^2	H_{UVW2} (kpc)	χ^2	H_{FUV} (kpc)	χ^2	d.o.f.
Late-type Galaxies									
NGC 3079	2.9 ± 0.3	15.6	3.5 ± 0.5	0.56	5.1 ± 1.5	0.80	4.5 ± 0.1	17.8	3
NGC 5775	2.4 ± 0.3	3.5	3.0 ± 0.2	10.7	2.65 ± 0.08	4.6	3.4 ± 0.1	15.9	8
NGC 5907	2.7 ± 0.4	1.3	2.2 ± 0.3	1.45	3.0 ± 0.7	0.53	2.32 ± 0.03	22.5	8
Early-type Galaxies									
NGC 3613	6.9 ± 0.1	5.8	7.8 ± 0.2	27.4	6.0 ± 0.2	16.2	6.1 ± 0.1	2.3	6
NGC 4594	3.5 ± 0.1	4.2	2.8 ± 0.3	2.2	3.1 ± 0.3	4.0	3.07 ± 0.05	3.7	8
NGC 5866	2.0 ± 0.1	1.5	2.5 ± 0.4	7.5	4.0 ± 1.5	0.11	2.0 ± 0.1	17	4

Note. — Scale heights are measured by fitting exponential profiles $I_0 e^{-z/H}$ to the data averaged over both sides of the midplane, where z is the projected distance above the midplane.

2006). The scale height of the H I, where it has been measured (e.g., Fraternali et al. 2002; Oosterloo et al. 2007; Kamphuis 2008) is comparable but systematically lower (1–2 kpc) than UV values, probably because we start measuring at larger heights to avoid stars.

For the galaxies where H cannot be measured, the maximum extent of the emission z_{max} in each band is a useful proxy for the observable halo size. We define z_{max} as the mean height above the midplane for which we detect flux at 2σ on both sides of the galaxy. Because of real angular variation in the sky foreground (which dominates σ_{sky} , there is a natural limit to the halo flux that can be detected; additional exposure time may detect some emission beyond z_{max} , but not much. Within z_{max} , additional exposure time improves the S/N and allows smaller flux measurement box sizes.

The z_{max} values are tabulated in Table 6 for the non-*uvw1* filters. The final column is the average z_{max} for the NUV, *uvm2*, and *uvw2* filters, which gives a measure of the maximum detectable emission at or above 2000 Å. The left panel of Figure 13 shows $z_{\text{max,FUV}}$ as a function of the average NUV $z_{\text{max,2000}}$. Spiral galaxies are represented as blue squares, S0 as black triangles, and elliptical galaxies by red diamonds. The “error bars” show the width of the flux measurement bin for each galaxy, and the line shows where a galaxy would fall if the FUV z_{max} were equal to $z_{\text{max,2000}}$.

All of the spiral galaxies except for NGC 4173 have $z_{\text{max,FUV}} \geq z_{\text{max,2000}}$, whereas the ellipticals fall below this line. The S0 galaxies also tend to fall below or on the line. Since spiral and elliptical galaxies overlap in specific halo UV luminosity (see the right panels of Figure 12) and scale height (Table 5), the observation that the FUV flux falls less rapidly than the other bands among the spirals and more rapidly among the early-type galaxies hints at a different origin.

A difference can also be seen in the ratio of the FUV and NUV fluxes as a function of height above the midplane, normalized to z_{max} (the right panel of Figure 13). There is a clear separation between the spirals and E/S0 galaxies, but notably the S0 galaxies differ from the elliptical galaxies in that the FUV/NUV ratio is roughly constant with height, whereas in the ellipticals it drops (however, there are only four elliptical galaxies in our sample).

4.2.3. Spectral Energy Distributions

Table 6
Maximum Extent of UV Halo Emission

Galaxy	Binsize (kpc)	NUV (kpc)	<i>uvm2</i> (kpc)	<i>uvw2</i> (kpc)	FUV (kpc)	$z_{\text{max,2000}}$ (kpc)
ESO 243-049	6.6	13.2	13.2	13.2	13.2	13.2
IC 5249	1.7	4.8	3.1	3.1	4.8	3.7
NGC 24	1.1	5.9	3.7	3.7	4.8	4.4
NGC 527	3.0	7.5	7.5	10.5	7.5	8.5
NGC 891	2.1	5.4	7.5	9.7	7.5	7.5
NGC 1426	1.3	16.2	9.8	5.7	3.2	10.6
NGC 2738	3.3	5.0	5.0	5.0	5.0	5.0
NGC 2765	1.8	10.9	12.7	10.9	7.2	11.5
NGC 2841	1.8	16.6	14.9	7.9	14.9	13.1
NGC 2974	3.5	17.5	10.5	14.0	7.0	14.0
NGC 3079	2.5	14.8	12.2	14.8	14.8	13.9
NGC 3384 ^b	1.1	>4.0	>5.0	>4.0	2.8	>4.3
NGC 3613	2.2	14.1	20.7	20.7	12.0	18.5
NGC 3623 ^a	0.88	7.4	7.4	6.6	7.4	7.1
NGC 3628	2.0	7.5	9.5	7.5	11.5	8.2
NGC 3818	2.0	12.0	10.0	8.0	4.0	10.0
NGC 4036	1.5	5.3	6.8	8.2	6.8	6.8
NGC 4088	2.2	12.4	12.4	10.1	12.4	11.6
NGC 4173 ^a	1.1	3.1	3.1	6.5	3.1	4.2
NGC 4388	2.5	8.0	10.0	10.0	10.0	9.3
NGC 4594	1.0	12.5	8.5	7.5	10.5	9.5
NGC 5301	1.8	9.6	9.6	6.1	9.6	8.4
NGC 5775	1.8	13.4	15.2	15.2	17.0	14.6
NGC 5866	1.0	7.5	7.5	7.5	6.5	7.5
NGC 5907	1.5	6.8	5.2	6.8	15.8	6.3
NGC 6503 ^a	0.5	3.3	2.3	5.8	3.8	3.8
NGC 6925	2.0	12.0	10.0	12.0	12.0	11.3
NGC 7090	-	-	6	6	-	6
NGC 7582	3.0	7.5	7.5	16.5	10.5	10.5
UGC 6697	-	17	-	17	23	17
UGC 11794 ^a	4.0	14.0	14.0	10.0	14.0	11.3

Note. — We obtain a crude measurement of $z_{\text{max},i}$ of the halo emission in each filter i by finding the height above each galaxy z where there is at least a 2σ detection in both extraction bins at z . The final column is the mean z_{max} for the NUV, *uvm2*, and *uvw2* filters.

^a Flux was only measured on one side of the galaxy.

^b The galaxy was on the chip edge.

In the third column of Figures 7, 8, 9, and 10, we show the four-point SED as a function of height above the midplane for each galaxy based on the fluxes in the middle column of the same figures. The SED of the galaxy itself (scaled to fit on the plot) is shown as a dotted line at the top of each panel, and the *uvw2* data points have been corrected using the correction factor listed in Table 4. The galaxy SEDs have not been corrected for extinction within the galaxy.

There are several remarkable features of the SEDs. First, the halo SEDs around most late-type galaxies and some of the S0 galaxies differ markedly from the galaxy

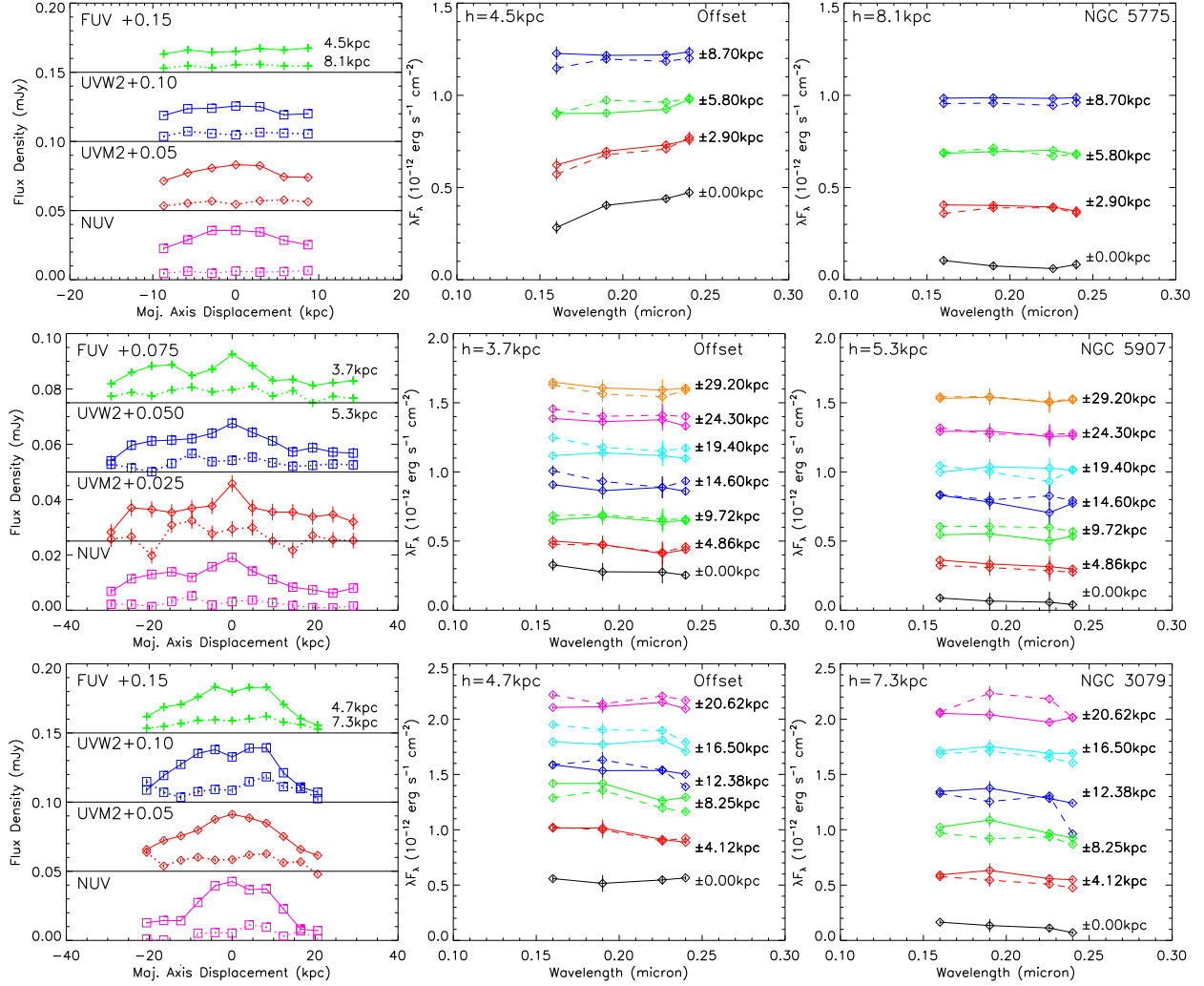


Figure 14. Variation in halo emission as a function of displacement along the projected major axis for NGC 5907, NGC 5775, and NGC 3079. The left panel shows the flux profile along the major axis at two heights above the midplane (averaged over both sides along the minor axis). The solid and dotted lines show the profile at two different offsets along the minor axis. The UV SEDs at each height above the major axis are shown at center and right. In all panels, we have added artificial offsets for visual clarity and show the SED on both sides of the midplane (solid and dashed lines) at each major axis offset (different colors). See text for discussion.

SED, whereas the SEDs of the elliptical galaxies (Figure 10) appear similar near and far from the nucleus. The halo emission is different from the integrated starlight of the galaxy. Second, the halo SED appears to be connected to the galaxy type.. Most Sc and Sb galaxies (Figures 7 and 8) have halo SEDs that are either flat or decline from the FUV to NUV, while elliptical galaxies have “halo” SEDs that rise from the FUV to NUV. Third, we do not find any systematic differences due to inclination in disk galaxies. This suggests that the SEDs measured in galaxies of lower inclination are from the halo rather than an outer spiral arm (i.e., an XUV disk). Finally, the halo SEDs of the S0 galaxies (Figure 9) do not have an archetypal shape. In some cases the SED rises continuously from the FUV through the NUV, whereas in others the NUV flux is lower than the *uvm2* flux. This does not seem to depend on the SED of the galaxy, and the SED may turn over with increasing height.

The ratio of halo flux to galaxy flux varies substantially

between galaxies, but is typically a few percent or less for the late-type galaxies while it ranges from 10–100% for the early-type galaxies (average 25% for S0s and 45% for ellipticals). The FUV fluxes and SEDs of the elliptical galaxies indicate that none of the ellipticals in the sample is a “UV upturn” galaxy (e.g., Code & Welch 1979; Burstein et al. 1988; Yi et al. 2011) where the FUV luminosity is larger than the NUV luminosity and the UV flux rises between 2500Å and the Lyman limit.

4.2.4. Variation along the Major Axis

Some of the data allow us to measure the flux as a function of displacement along the projected major axis as well as projected height above the galaxy. Figure 14 shows the flux profiles along the major axis at two different heights for three of the galaxies with the best data. The fluxes in each band are shown with an artificial offset for clarity. The bins closest to the galaxy follow a typical trend where a central enhancement is visible and the flux declines to larger displacements (except the FUV band

in NGC 5775), but higher above the galaxy the profile is much flatter. In NGC 5907 and NGC 3079, we measure more flux on one side of the galactic center than the other. In the galaxies shown here (especially NGC 5907) most variations along the major axis are correlated between filters; this may be due to where star formation occurs in the disk or the structure of the halo or cirrus substructure.

The SEDs at each height are shown in the right two panels of Figure 14 (with artificial offsets) and show that while there is general agreement on each side of the galactic center there are real variations. Again, it is not clear whether the source is halo structure, variation in the disk, or cirrus. Notably, the SED of NGC 5775 flattens out at large displacement. This may be due to the rapid, but “distributed” star formation in the galaxy (producing a bluer spectrum at larger offsets), or perhaps due to extinction within the halo itself modifying the observed spectrum. In the other two galaxies, the increased flux near the disk does not have a strong effect the SED as a function of displacement, except near $R = 0$ in NGC 3079.

Similar trends are seen in other galaxies in our sample which have deep data in fewer than three filters. At any given height, differences as a function of displacement are usually visible in more than one band, so the background is low enough to permit searches for halo substructure.

4.3. Comments on Individual Galaxies

Cirrus around NGC 891, NGC 3623, and NGC 6925—Galactic cirrus is in virtually every field, but for most of the sample the contribution is small and the variation across the field is slight. The cirrus is faint and can only be seen in heavily smoothed, stretched images (it cannot be seen in the galaxy images presented in this work), but it can be brighter than the halo light. Some galaxies cannot be used at all because of the cirrus (e.g., NGC 7331), but there are several borderline cases. NGC 891 has more cirrus emission on the west side of the galaxy (but the surface brightness is still very low relative to the galaxy). This was partially corrected by using different background regions on each side of the galaxy. NGC 3623 has spatially variable cirrus emission on the east side of the galaxy, but no visible cirrus on the west side, so we measure fluxes only on this side. NGC 6925 is in a region of patchy cirrus with stronger emission on the east side, which may explain the irregular appearance of the halo flux profile (Figure 8).

NGC 2974—NGC 2974 is classified as an E4 galaxy, but the *GALEX* data (described in detail in Jeong et al. 2007) reveal a blue star-forming ring in the galaxy. However, this ring does not seem to differentiate the halo emission from NGC 2974 from the other elliptical galaxies (Figure 10) except in the innermost bin, where the relative FUV flux is higher.

IC 5249, NGC 24, NGC 6503, and NGC 4173—These galaxies are significantly smaller than the other spiral galaxies in our sample, and were included because they met our cutoff criteria and had good *Swift* data. Their inclusion in the sample is useful since they demonstrate that UV emission around smaller galaxies has the same general character as that from the large ones.

NGC 24 and NGC 6503 have large UV halos for their specific SFR relative to the other galaxies in the sample (on absolute scales, they are smaller than the halos of the more massive galaxies). NGC 4173 also has a relatively large halo, assuming it is indeed at 8 Mpc, where its $M_K = -18$ mag indicates a stellar mass of $M_{\text{star}} \sim 3 \times 10^8 M_{\odot}$. We are only able to measure the halo emission to one side of NGC 4173 because of the members of HCG 061 to the south; NGC 4173 was originally classified as a member of HCG 061 (HCG 061b), but it is known to be a foreground object. IC 5249 has a smaller halo.

Since z_{max} does not scale with the angular size of the galaxy for these or other galaxies in our sample, it seems likely that this is a real effect, but the reason for the large UV halos is not clear, since the small galaxies do not have unusually high specific L_{ν} . One possibility is that the galaxies have less extinction in the disk. Another is that the galaxies have large dusty halos despite their smaller stellar mass relative to the rest of the sample. Data for more small galaxies are required to determine how z_{max} is related to galaxy mass and other parameters.

NGC 24 is remarkable in that it has very high quality *Swift* data. Its flux height profile and SED (Figure 7) look very similar to other spiral galaxies with very deep data, suggesting that all star-forming late-type galaxies have similar UV halos.

UGC 6697, UGC 11794, NGC 527, and ESO 243-049—Most of our sample is restricted to $d < 50$ Mpc because the angular sizes of the halos become too small to use multiple flux measurement boxes. However, for galaxies with sufficiently deep data it may be possible to measure a halo size.

We detect halos out to about the same distances from the midplane, but as a result of the larger physical sizes of the bins, we only see the halo emission in the two innermost bins. If these galaxies are representative of galaxies at $50 \text{ Mpc} < d < 100 \text{ Mpc}$, halo detection should be straightforward but the maximum extent, SED, and total flux will depend strongly on the bin sizes used and are more sensitive to undetected point sources or background variations. Indeed, the profiles and SEDs for UGC 11794 and NGC 527 look more confused than the other galaxies in the sample, and for UGC 11794 it is questionable whether we see any halo emission.

5. HALO SEDS AND THE NATURE OF THE UV LIGHT

We now address the nature of the halo emission, which could either be intrinsic to the halo or a reflection nebula produced by scattering of UV photons that escape the disk. In the former case, starlight from the stellar halo is the most likely candidate (gas tends to be cold or very hot), so we expect SEDs and fluxes consistent with a stellar halo population. In the latter case, we expect the SED to be consistent with predictions using dust models and galaxy SED templates.

In this section, we examine which scenario is more consistent with the data from the perspective of UV- r color in the halo, SED fitting using dust models and galaxy template spectra, and leveraging the UVOT red leaks to predict a contribution from the stellar halo. We find that the UV light is more consistent with a reflection nebula for late-type galaxies, but that extended emission in el-

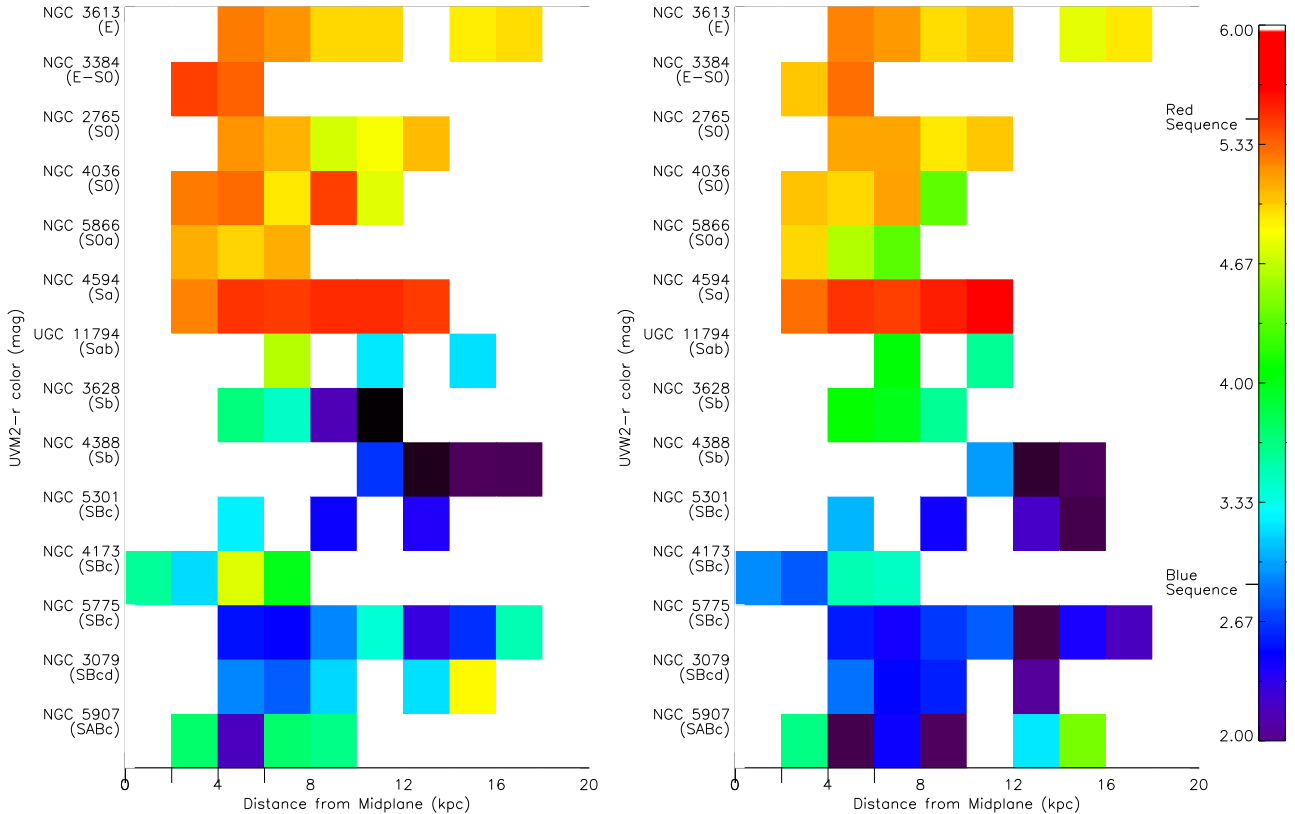


Figure 15. UV- r colors for the $uvm2$ and $uvw2$ filters for galaxies with SDSS r -band data. The galaxies are ordered from top to bottom in increasing morphological sequence. In each row, we show the UV- r color as a function of height above the midplane in 2 kpc bins, where the UV- r color is in magnitudes and colored according to the colorbars on the right, which were generated based on the magnitudes in Wyder et al. (2007). See Section 5 for additional details.

lptical galaxies is probably from stars in the outskirts.

5.1. UV- r Color

If the UV light is consistent with a single-population stellar halo, we expect it to have a UV-optical color comparable to an early-type galaxy (perhaps bluer if the halo consists of metal-poor stars, but not as blue as a late-type galaxy).

We measured the UV- r colors using the $uvm2$, $uvw2$, and Sloan Digital Sky Survey (SDSS) DR7 (Abazajian et al. 2009) r bands for the diffuse emission. We use the UVOT rather than *GALEX* filters because of the better spatial resolution and the difficulty of removing the large-scale artifacts from the *GALEX* images (Section 3). We use the *uncorrected* $uvw2$ fluxes to eliminate potential bias, but note that this means the filter has an effectively longer central wavelength. The r -band flux was measured from source-free regions above the galaxy corresponding to the UV flux extraction boxes, and both the UV and r -band fluxes are converted to surface brightnesses (mag arcsec^{-2}).

Figure 15 shows the UV- r colors for the two bands as a function of height above the midplane along the x -axis and as a function of increasing morphological type along the y -axis. Only galaxies with suitable SDSS data are included. The UV- r color (in magnitudes) is encoded as an RGB color based on the UV- r color-magnitude

diagram (CMD) from Wyder et al. (2007), i.e., a blue color corresponds to a galaxy on the blue sequence and a red color to a galaxy on the red sequence in their CMD. Wyder et al. (2007) based their CMD on *GALEX* data, so we computed a small magnitude shift due to the difference in filters. Figure 15 is *not* itself a CMD, but one can see a clear dichotomy among the early- and late-type galaxies. The blueness of the emission in the late-type galaxies indicates that the UV emission from late-type galaxy halos is not consistent with an older stellar population. In contrast, the redness of the emission above the early-type galaxies and the small extent of the FUV emission relative to the spirals (Figure 13) suggests that we are seeing the outskirts of the galaxy.

Figure 15 is imprecise. The coloring is based on the Wyder et al. (2007) CMDs, which are measured for *galaxies* rather than halos. There are also issues with measuring diffuse emission in the SDSS that add uncertainty to the r -band magnitudes, and the colors in the outer bins are unreliable. Still, the difference between early- and late-type galaxies is larger than the expected magnitude uncertainties (in total, less than 0.3 mag near the galaxy).

5.2. Fitting Reflection Nebula Models

If the halo light is a reflection nebula, then its spectrum will be the emergent galaxy spectrum modified by

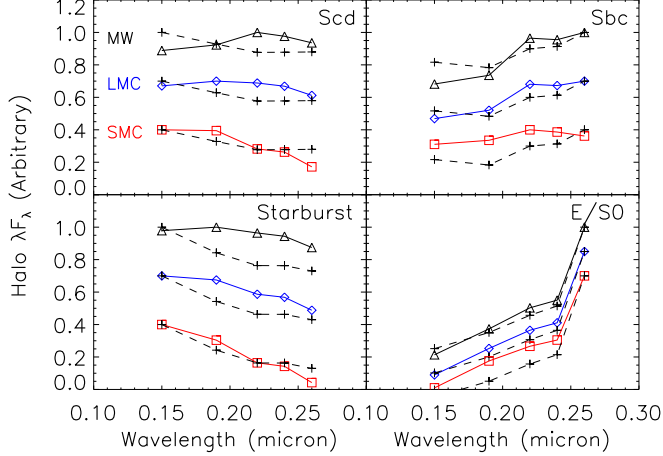


Figure 16. Model SEDs for four representative galaxy templates and MW, LMC, and SMC dust models, folded through the FUV, *wvw2*, *wvm2*, NUV, and *wvw1* filters. The NUV filter is plotted with an offset to 0.24 micron. The fluxes are a prediction of the halo emission in the reflection nebula scenario for each template, but note that the UV bump in the MW-type dust may not be real (see text).

the dust in the halo. Here we test this scenario by fitting reflection nebula models (based on galaxy template spectra and Local Group dust models from WD01) to the measured halo SEDs (from fluxes in Table 4).

Even if the UV halos are reflection nebulas, we do not know the dust type or the galaxy spectrum as seen by the halo (the galaxies are highly inclined), so we do not expect our models to produce formally good fits in many or most cases. To provide context, we fit each halo SED with a suite of reflection nebula models produced for several galaxy types and dust models. A good or marginal fit for a model constructed from the “right” galaxy template and dust model that is significantly better than fits with other models would support the reflection nebula hypothesis (but not rule out other, non-reflection nebula models).

5.2.1. Model SEDs

For an optically thin halo with a single type of dust, the scattered spectrum is

$$L_{\text{halo}}(\lambda) = L_{\text{gal}}(\lambda)(1 - e^{-\tau(\lambda)\varpi(\lambda)}) \quad (3)$$

where $\tau(\lambda) = N_H \delta_{\text{DGR}} \sigma_{\text{ex}}(\lambda)$ is the optical depth and $\varpi(\lambda) = \sigma_{\text{scat}}(\lambda)/\sigma_{\text{ex}}(\lambda)$ is the scattering albedo. N_H is the column density of hydrogen, δ_{DGR} is the dust-to-gas ratio, and $\sigma_{\text{ex}}(\lambda)$ is the extinction cross-section for a given dust mixture. $\sigma_{\text{ex}}(\lambda)$ and $\varpi(\lambda)$ come from a dust model. L_{halo} and L_{gal} are measured quantities, so if one knows two of the constituents of $\tau(\lambda)$, the UV measurements yield the third. In our case, we know neither N_H nor δ_{DGR} , but these do not affect the spectrum (assuming an optically thin halo). Thus, we can fit each model SED to the halo SED with the dust column $N_d = N_H \delta_{\text{DGR}}$ as a free parameter.

If $\tau \ll 1$, then $L_{\text{halo}} \approx L_{\text{gal}} \tau \varpi$. This depends on N_H and δ_{DGR} , since $\sigma_{\text{ex}} \delta_{\text{DGR}} \sim 10^{-21} \text{ cm}^2$ and $\varpi \lesssim 0.5$ between 1500–3000Å for dust models based on Local Group dust. It is difficult to separate the truly extraplanar gas from the disk gas, which has a finite height, without a

fully 3D view of the galaxy, but here we loosely define the halo as a region above several optical scale heights (as seen around edge-on systems), which is where we measure the UV light. In practice, this means a few kpc. At this height, $N_H \sim 0.1 - 1 \times 10^{20} \text{ cm}^{-2}$ around many Milky Way-sized edge-on galaxies (e.g., Sancisi et al. 2008, and references therein). Since the extraplanar H I at a few kpc from the midplane or above is typically consistent with an exponential atmosphere, the mean column from the “bottom” of the halo to infinity is perhaps 10^{20} cm^{-2} (L_{gal} must then also be defined as the emergent galactic light at this height). For the $\delta_{\text{DGR}} \sim 1/100$ in the Milky Way (and galaxy halos; Ménard & Fukugita 2012), this means $\tau \lesssim 0.1$ and the optically thin approximation is valid.

This implies a $L_{\text{halo}}/L_{\text{gal}}$ ratio of a few percent for $\varpi \lesssim 0.5$. We discuss this in detail in Section 6, but here the relevant point is that the attenuation of the reflection nebula spectrum by dust in the halo is less than 10%, and often much less because by the time a typical photon has scattered it will have passed through the densest region of the halo and scattering is highly forward-throwing (Draine 2003). In other words, the scattered light we see at any point in the halo was largely traveling outwards and thus sees a smaller τ on the way out of the halo. A self-consistent Monte Carlo radiative transfer scheme is required to rigorously compute the reflection nebula spectrum (including a disk emission model, halo model, and dust model), and this will be the subject of a future paper. However, we expect the extinction of the reflection nebula spectrum in the halo is between 1–5%, which is smaller than the error on the measured fluxes. Thus, the effect will not be discernable in our fitting.

Our model spectra consist of galaxy templates and Local Group dust models from WD01. We used galaxy templates for the input spectra because the sample galaxies are highly inclined and a detailed model is required to de-redden them. For the spiral galaxies we used six templates, including Bolzonella et al. (2000) templates for the Sbc and Scd galaxies (denoted as BMP Sbc and BMP Scd respectively) and the Kinney et al. (1996) templates (starburst2, Sc, Sb, and Sa), which we denote as KC SB2, KC Sc, KC Sb, and KC Sa respectively. The different starburst templates are based on different levels of internal extinction, and for our sample a low level is appropriate (the starbursts in the sample are not luminous infrared galaxies). For the early-type galaxies we used the Kinney et al. (1996) and Bolzonella et al. (2000) templates (denoted KC E and BMP E).

Figure 16 shows model SEDs for four galaxy templates with the MW ($R_V = 3.1$), LMC average, and SMC bar dust models from WD01. In each panel, we show the models and a raw template spectrum normalized to their maxima in order to show the differences. The LMC and SMC models have offsets for visual clarity. While models with MW and LMC dust appear redder than the input spectrum in this wavelength range, the SMC dust model is bluer. The region of the spectrum near the 2175Å UV bump is unreliable. The bump is thought to be purely absorptive (Andriess et al. 1977; Calzetti et al. 1995, also A. Witt 2014, private communication) because of the size of the grains that produce it. Although the WD01 model does show the bump is primarily absorptive (cf. Draine

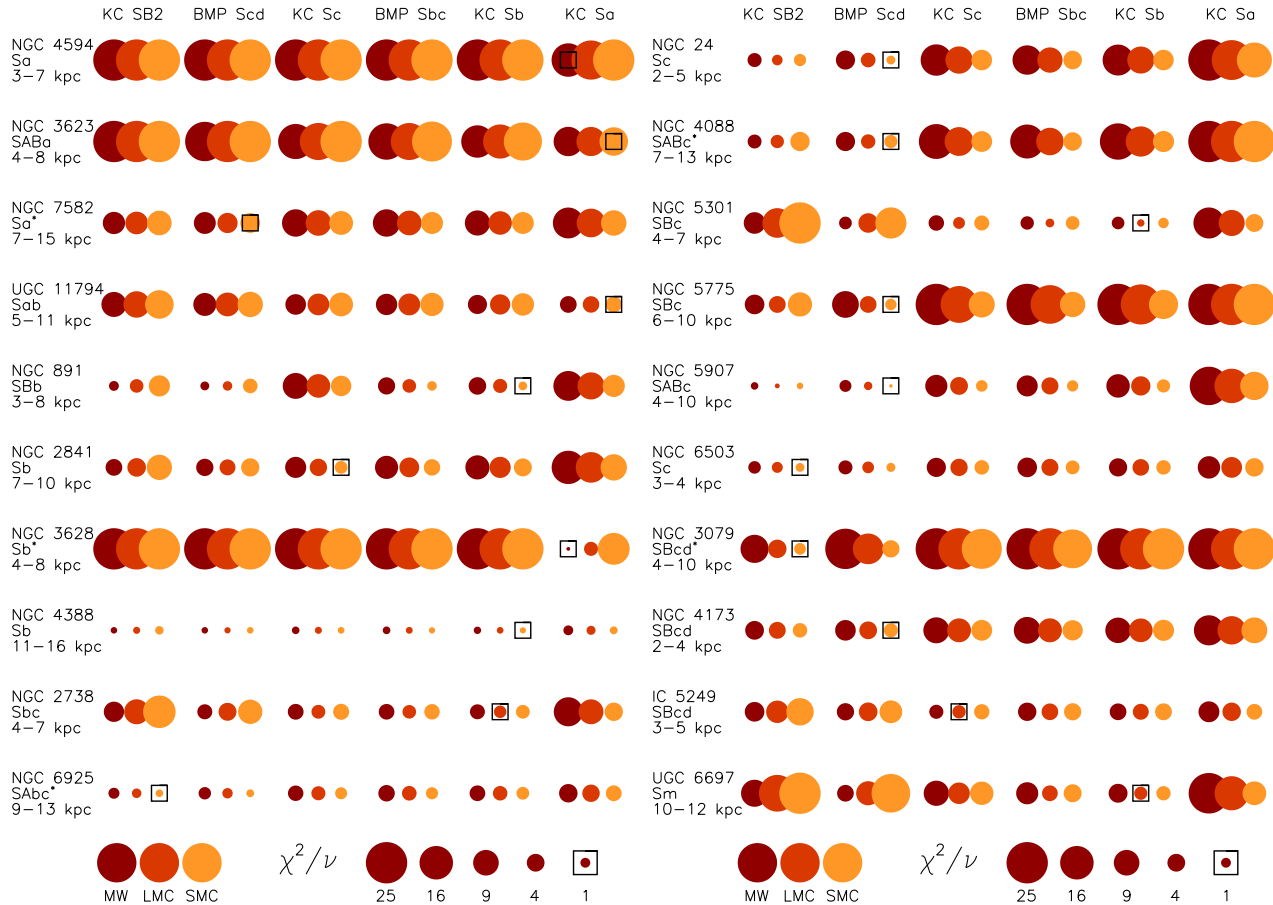


Figure 17. Reflection nebula model fits for the spiral galaxies as a function of galaxy template and dust model used. MW-, LMC-, and SMC-type dust are shown as dark red, orange, and light orange respectively. The reduced χ^2 values (clipped at 25) are shown as different sizes of circles, and the best-fit model for each galaxy is enclosed in a box. Asterisks denote starburst galaxies, and we give the height where the SED was measured. The templates are the Kinney et al. (1996) starburst2, Sc, Sb, and Sa (KC SB2, KC Sc, KC Sb, and KC Sa) and Bolzonella et al. (2000) Scd and Sbc (BMP Scd and BMP Sbc) models. See text for discussion.

2003), ϖ is a derived quantity in their models and there is a small residual bump that may indicate a small inaccuracy. Thus, the peak seen in the *uvm2* filter for the MW model (and, to a lesser extent, the LMC model) in the Scd and Sbc models may be inaccurate. However, the LMC and SMC dust are adequate representations of a scattered spectrum for testing whether the halo light is consistent with a reflection nebula. Thus, in the reflection nebula scenario we expect the best fits with LMC- or SMC-type dust and a galaxy template that matches the galaxy type.

5.2.2. Fitting Results

We fit the measured halo SED using least-squares fitting with the χ^2 goodness-of-fit statistic. The measured SEDs come from the fluxes in Table 4, and the *uvw1* filter is not used because of the red leak (we return to this later). It is also formally inappropriate to use the *uvw2* correction factor, which depends on the true underlying spectrum, but for these fits the difference in correction factor between galaxy templates is only a few percent after the dust model has been folded in because extinction is much more efficient in the UV.

Figure 17 shows χ^2/ν for the best-fit scaling factor in

each model for the spiral galaxies. The left-hand panel shows the Sa–Sbc galaxies, and the right-hand panel the Sc–Scd galaxies. In each row, we show the χ^2/ν values for the best fit for each model, where there are three circles per template representing (from left to right) the χ^2/ν value for MW, LMC, and SMC-type (dark red, orange, and light orange) dust models respectively. The best fit overall for each galaxy is marked by a box, and the values are encoded as circles whose sizes correspond to χ^2/ν , which is clipped at 25. Smaller circles are better fits. We omit the early-type templates, but these are never preferred.

The best 2–3 fits typically occur for a galaxy template close to the host galaxy type (Figure 17, note that an asterisk after the galaxy type denotes a starburst), and the best-fit model uses the SMC or LMC dust in 18/20 cases. If we consider only those cases where $\chi^2/\nu \leq 3$, 9/11 use the SMC model, which we think has the most accurate ϖ of the WD01 models. For most galaxies the fit gets significantly worse as the template becomes a worse match to the galaxy type if we use the MW dust model. An obvious exception is NGC 3628 (Figure 17), whose halo SED is closer to an Sa type galaxy (Figure 8).

Only a few of the early-type galaxies in the sample have

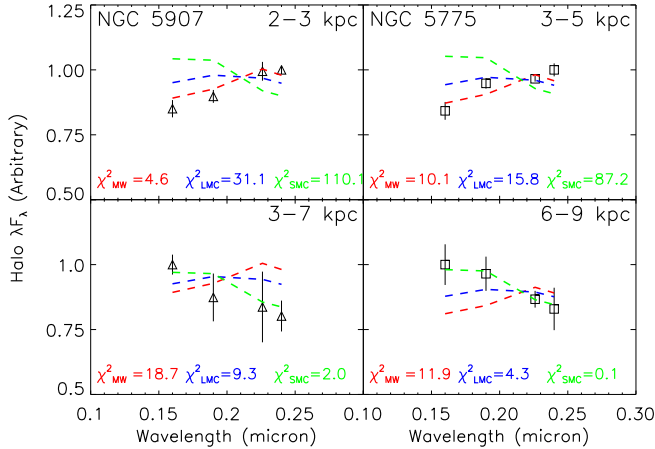


Figure 18. Measured SEDs and the best-fit models (using the BMP Scd template) for two zones around NGC 5907 and NGC 5775. Closer to the galaxy, the SED is more consistent with MW or LMC-type dust, whereas the slope reverses farther out and SMC-type dust is a better fit. This is true of other late-type galaxies in the sample, but the data are not as good.

“halo” emission that is fit well by any of the reflection nebula models (not shown). In most cases, the observed SED rises continuously towards longer wavelengths and the FUV emission is too weak to obtain $\chi^2/\nu \lesssim 25$.

Some halo SEDs get bluer farther from the galaxy, and a few galaxies have data of sufficient quality to measure a change in the SED slope. Figure 18 shows the SED measured near and farther from the galaxy for NGC 5907 and NGC 5775, where the sign of the slope reverses from closer to the disk (though still several kpc above the midplane) to farther out. We have also plotted the best-fit models for each dust model using the BMP Scd template. The SEDs closer to the disk cannot be fit well with a reflection nebula model, whereas the SEDs higher up are fit very well by the SMC model. Thus, near the disk there may be an additional component or the reflection nebula model is invalid. Extinction of a reflection nebula *by dust in the halo* cannot explain the change in slope, as the required N_H is several $\times 10^{22} \text{ cm}^{-2}$ (for $\delta_{\text{DGR}} \sim 1/100$). A similar transition is also seen in NGC 891 and NGC 5301, but not in NGC 3079 (or NGC 24 and NGC 4088, which are less inclined, so the halo extraction boxes slice through multiple heights).

We note that the SMC δ_{DGR} is 5–10 times smaller than in the Milky Way (depending on the region; Gordon et al. 2003; Leroy et al. 2007), so for SMC dust the implied N_H to produce a given L_{halo} is likewise higher. However, Ménard & Fukugita (2012) found $\delta_{\text{DGR}} = 1/108$ for the halo dust with an SMC-like extinction curve (i.e., a similar dust composition to the SMC but a different δ_{DGR}). Using their value, we find a mean $N_H \sim 5 \times 10^{19} - 3 \times 10^{20} \text{ cm}^{-2}$ based on Equation 3. For truly SMC dust, the value is commensurately higher. The column density through the halo is discussed in more detail in Section 6.

5.3. The UVOT Red Leaks

The UVOT red leak means that the *uvw1* and *uvw2* filters have redder central wavelengths than the nominal values. The effect is stronger in the *uvw1*, which we ex-

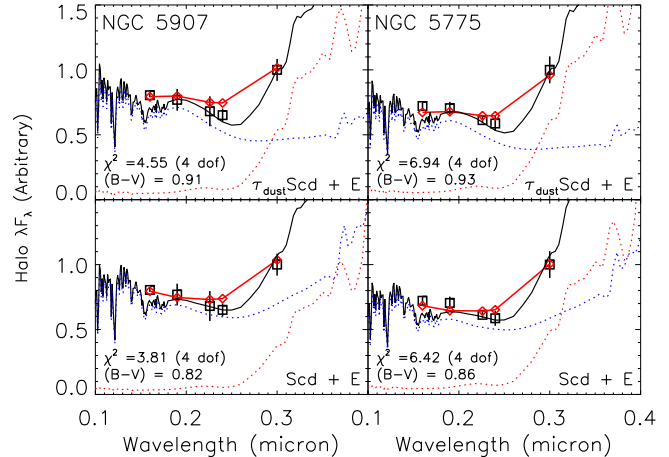


Figure 19. SEDs including the *uvw1* filter (black) with best-fit reflection nebula+BMP elliptical template model (top panels) and BMP Scd+elliptical template model (bottom panels) for NGC 5907 and NGC 5775 (solid red line). The model λF_λ is overplotted in arbitrary units (not a fit) with the proportional components shown as dotted blue (reflection nebula or Scd template) and red (elliptical template) lines. The *uvw1* flux is plotted at the effective wavelength computed for that model, not its nominal wavelength of 2600Å. See text for discussion.

cluded from our SED fitting. The best-fit models for the 4-point SEDs all underpredict the measured *uvw1* flux for the spiral galaxies, so the proportion of excess flux tells us about the luminosity of another component. If the second component is a (classical) stellar halo and the reflection nebula hypothesis is correct, we expect the model to fit well when the stellar component has about the same luminosity (and perhaps color) as observed halos.

We attempted to determine the stellar halo luminosity in this way for NGC 5907 and NGC 5775, which have some of the best data. For the reflection nebula component, we used the best-fit models from above, and for the stellar halo we tried the elliptical galaxy templates from above as well as GALEV (a population synthesis and evolution code; Kotulla et al. 2009) E/S0 and Sa models with metal-poor populations, which may better represent the stellar halo. We fit the halo model to measured SEDs including the *uvw1* flux, where the free parameter is the proportional flux in the stellar halo.

The best fits are shown in the top panels of Figure 19. The measured SEDs are shown as black boxes, and the best-fit model SED is shown as red diamonds connected by a red line. We have also overplotted the model λF_λ and its components (the dotted blue and red lines represent the reflection nebula and stellar halo respectively). The *uvw1* point is shown at an effective wavelength computed from the model and filter response. This wavelength is strongly model dependent. In both galaxies, the best stellar halo model is an early-type template rather than a metal-poor template, but the χ^2 values are not much different. For NGC 5775, $\chi^2/\nu = 1.7$, whereas for NGC 5907 $\chi^2/\nu = 1.1$ (NGC 5775 also has a worse χ^2 for the best fit in the prior subsection).

For NGC 5907, the model predicts a bolometric stellar halo luminosity of $2 \times 10^9 L_\odot$, and for NGC 5775 about $5 \times 10^9 L_\odot$. This is consistent with stellar halo measurements for these galaxies and with the Milky

Way (Carney et al. 1989), and stellar halos typically tend to have luminosities of a few percent of the host galaxy. We also computed the model $B - V$ colors by folding the spectrum through the B and V filters and adding a constant factor for comparison with observations, following Fukugita et al. (1995). The model $B - V$ color is 0.91 mag for NGC 5907 and 0.93 for NGC 5775. Lequeux et al. (1996) measured $B - V = 0.90$ for NGC 5907 (which is remarkable for being a “red” halo; Sackett et al. 1994), so for this galaxy the model is consistent with the observations.

We also tried fitting a dual stellar halo model, where the first component is simply a late-type galaxy template instead of the reflection nebula spectrum. This is motivated by the possibility that the UV light comes from halo stars of a separate population. Stars might form in some of the gaseous material expelled into the halo. Molecular gas has been seen up to a few kpc around some edge-on galaxies (e.g., Garcia-Burillo et al. 1992; Lee et al. 2002), and only a small amount of halo star formation is needed to explain the UV fluxes. For example, in NGC 891, the *GALEX* FUV halo flux integrated above 1 kpc requires a halo SFR of $\sim 0.028 M_{\odot} \text{ yr}^{-1}$ (using the formulas in Kennicutt 1998; Parnovsky et al. 2013). We would expect some associated $H\alpha$ emission, but NGC 891 has a bright $H\alpha$ halo; using the scale height of 520 pc and total $L_{H\alpha} \sim 9 \times 10^{40} \text{ erg s}^{-1}$ from Howk & Savage (2000), the diffuse $H\alpha$ above 1 kpc is over 7 times higher than that expected from halo star formation.

The dual halo model provides equally good fits (bottom panels of Figure 19), but the luminosity of the redder halo is several times smaller than for the reflection nebula (plus halo) model, and the $B - V$ colors are bluer. The reflection nebula and stellar halo model predicts more realistic stellar halos.

There are several other galaxies where we can do similar fits: NGC 24, NGC 891, NGC 2841, and NGC 5301. In each case, 80–85% of the flux in the best-fit models comes from the reflection nebula component in that model, with $B - V \sim 0.84 - 0.93$. The early-type galaxies, by comparison, have *uvw1* fluxes consistent with the outskirts of the galaxy.

5.4. Maximum Extent of the FUV Emission

In Section 4, we noted that around spiral galaxies the FUV emission is visible at least as far or farther than emission in the other bands, whereas in elliptical galaxies the FUV emission drops below 2σ before the other bands (Figure 13). This is probably not due to a difference in scale height between bands (e.g., Table 5) but rather a difference in SED and emission mechanism.

The extent of the FUV emission is simply explained in the reflection nebula scenario by the relatively large FUV flux emerging from star-forming galaxies as well as the higher scattering cross-section at shorter wavelengths. A traditional stellar halo (even a metal-poor one) is not likely to be more detectable in the FUV than other bands. If the light is from younger stars, the scale heights of 3–5 kpc for NGC 3079, NGC 5775, and NGC 5907 indicate that there are some young stars over 10 kpc from the disk.

5.5. Summary and Caveats

In late-type galaxies, the reflection nebula model is a better explanation than a stellar halo for the UV halo SED. We have considered the UV– r colors in the halo and the halo SEDs. The early-type galaxies, on the other hand, have UV– r colors and SEDs in their “halos” that are consistent with being the faint galactic outskirts rather than a reflection nebula. The S0 galaxies have some distinct halo emission (the halo SEDs differ from the galaxy and the FUV emission extends far from the galaxy), but additional data are required to separate the light from the stellar halo/galaxy outskirts.

We caution that we have not tried models other than the reflection nebula, classical stellar halo, and two-component stellar halo, so our results do not prove a reflection nebula origin. Even if the UV halo is a reflection nebula, the dust model we used may not be accurate. A better dust model (perhaps patterned after Nozawa & Fukugita 2013), including Monte Carlo radiative transfer, is required to make stronger statements about the dust content, and will be the subject of a future paper.

6. COMPARISON WITH OPTICAL REDDENING FROM MSFR10

In the reflection nebula picture, the ratio of the halo and galaxy luminosity depends on the amount of dust (Equation 3). Since the halo dust also reddens background sources, we can determine whether the UV data are consistent with the dust that produces the extinction measured by MSFR10 at larger radii by comparing the halo luminosity and light profile we expect if the MSFR10 results are extrapolated to smaller radii.

MSFR10 fit a curve to the mean extinction as a function of projected galactocentric radius, r_p . In this section, we first derive the volume density profile implied by the MSFR10 fit, which is required to measure extinction within the halo. We then compute a plausible range of $L_{\text{halo}}/L_{\text{gal}}$ values for such a halo, using the WD01 SMC dust model that we think best approximates the scattered spectrum with the δ_{DGR} from Ménard & Fukugita (2012). Comparing this range to the observed data requires several additional considerations, such as the distributed nature of the galaxy emission, the anisotropy of scattering, and accounting for the extinction in the disk for estimating L_{gal} . We adopt a simplistic model (a more realistic model is reserved for a future paper) to show that the data are consistent with the halo luminosity expected from the MSFR10 profile at small radii. Finally, we compare the height profile of the measured UV fluxes to that expected from the MSFR10 curve and compute the gas mass.

We focus on the *uvm2* data, where there is no contamination from the stellar halo and where we think the background is the most uniform. However, the analysis could be extended to the other bands.

6.1. A Spherical MSFR10 Halo

MSFR10 fit a curve to the mean optical extinction in the V band, $A_V(r_p)$, towards background sources with $r_p = 15 - 1000 \text{ kpc}$ (Equation 30 in their paper). $A_V(r_p)$, depends on the projected column density $N_{H,\text{proj}}(r_p)$

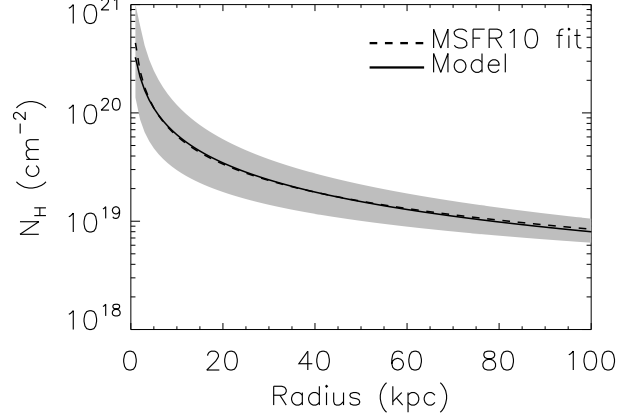
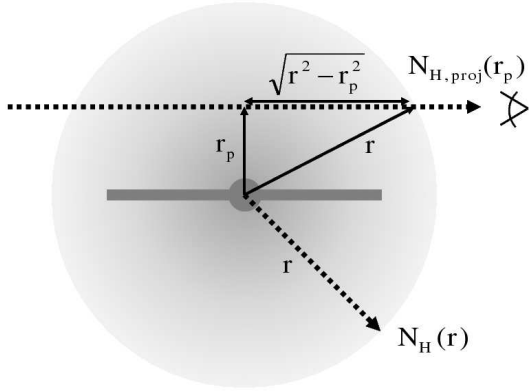


Figure 20. *Left:* Cartoon of a spherical halo showing the relationship between N_H measured by an observer and N_H from the origin through the halo. *Right:* MSFR10 fit a curve to their mean $A_V(r_p) \propto N_H(r_p)$ measurements (dashed line, 1σ error shown in grey) that is consistent with a volume density $n(r) \propto r^{-1.96}$ (solid line). See text for discussion.

through the halo and the dust model:

$$\begin{aligned} A_V(r_p) &= 0.23 \pm 0.06 \left(\frac{r_p}{1\text{kpc}} \right)^{-0.86 \pm 0.19} \\ &= 1.086 \sigma_{\text{ex}}(V) \delta_{\text{DGR}} N_{H,\text{proj}}(r_p) \end{aligned} \quad (4)$$

where $\sigma_{\text{ex}}(V)$ is the extinction cross-section in the V band.

If the halo of dust-bearing gas is spherically symmetric, we can use $N_{H,\text{proj}}(r_p)$ to obtain the volume density as a function of galactocentric radius r (Figure 20). From $n(r)$, we can then find the column density between the center of the halo and a point within, $N_H(r) = \int n(r) dr$. $N_{H,\text{proj}}(r_p)$ is integrated through the halo on a path perpendicular to r_p (see Figure 20), i.e., $N_{H,\text{proj}}(r_p) = \int n(s) ds$. The integral is effectively over all volume densities $n(r > r_p)$ and the path length from r_p to some higher r along the path is $s = \sqrt{r^2 - r_p^2}$. Thus,

$$\begin{aligned} N_H(r_p) &= \int n(s) ds = 2 \int_{r_p}^{\infty} n(r) \frac{r}{\sqrt{r^2 - r_p^2}} dr \\ &= \frac{A_V(r_p)}{1.086 \sigma_{\text{ex}} \delta_{\text{DGR}}} \end{aligned} \quad (5)$$

It is possible that $n(r)$ does not have an easily integrable form, but based on the MSFR10 fit a reasonable choice is $n(r) = n_0 r_{\text{kpc}}^{-x}$, where x is determined by choosing a value, evaluating the integral, and comparing the resulting $N_{H,\text{proj}}(r_p)$ to the MSFR10 curve. The best-fit exponent is $x = 1.96 \pm 0.06$, which is consistent with $x = 2$ within the MSFR10 error bars (Figure 20). Thus, we adopt $n(r) = n_0 r_{\text{kpc}}^{-2}$. Since $n(r)$ diverges at $n = 0$, $N_H(r)$ is effectively normalized by some minimum radius,

$$N_H(r) = n_0 (1 \text{ kpc}) \left(\frac{1}{r_{\text{min}}} - \frac{1}{r} \right) \quad (6)$$

where the radii are in kpc. We do not know r_{min} , and in real galaxies the disk-halo interface is nebulous. Consid-

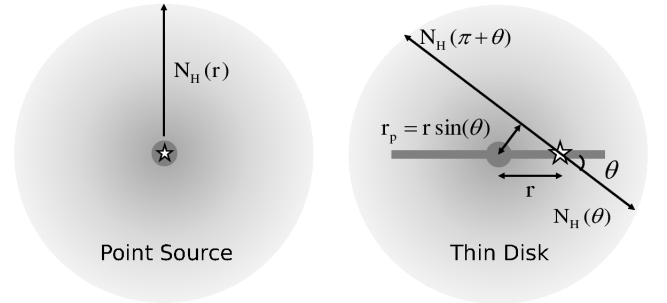


Figure 21. A “point source” galaxy and a uniformly bright disk in a spherical MSFR10 halo provide upper and lower bounds on the L_{halo} we expect because of the different mean column density. In the disk case, one can see that $N_H(\theta) + N_H(\pi + \theta) = N_{H,\text{proj}}(r \sin \theta)$ for a ray emerging at θ from a point source in the disk (right).

ering that thick (stellar) disks in disk galaxies have scale heights of 0.2 – 1.5 kpc (Yoachim & Dalcanton 2006), a reasonable choice of r_{min} is 2 kpc for Milky Way-sized disk galaxies, which is consistent with where we measure UV fluxes. Of course, a spherical halo model breaks down near the disk (extraplanar gas tends to look like an exponential atmosphere near the disk; e.g., Sancisi et al. 2008), so r_{min} could be thought of as a normalization. For $r_{\text{min}} = 2 \text{ kpc}$ and $\delta_{\text{DGR}} = 1/100$, the total N_H through the halo is a few $\times 10^{20} \text{ cm}^{-2}$. As N_H depends on δ_{DGR} but τ depends only on the dust column, we defer a discussion of N_H and gas mass to the end of this section.

The spherical halo described here (hereafter the MSFR10 halo) will be used through the rest of this section to estimate L_{halo} in the MSFR10 model, its light profile, and the total mass. We also assume that the halo is optically thin and that a scattered photon scatters only once before escaping, based on the N_H and $\delta_{\text{DGR}} \sim 1/100$. While the spherical approximation must break down near the disk, we will see below that it is useful.

6.2. $L_{\text{halo}}/L_{\text{gal}}$ in the MSFR10 Halo

$L_{\text{halo}}/L_{\text{gal}}$ can be derived in the MSFR10 halo from a dust model and a source/halo geometry. In this subsection, we determine the total luminosity and ignore the directional dependence in the scattering cross-section (which affects how much of the light is seen at a given viewing angle).

A ray traveling from the origin a distance r is attenuated by $e^{-\tau}$, where $\tau(r, \lambda) = N_H(r)\sigma_{\text{ex}}(\lambda)\delta_{\text{DGR}}$ (Equation 3). If $\tau \ll 1$ and we integrate over all rays to $r = \infty$, Equation 3 becomes

$$L_{\text{halo}}/L_{\text{gal}} \sim \tau(\lambda) = \overline{N_H}\sigma_{\text{ex}}(\lambda)\varpi(\lambda)\delta_{\text{DGR}} \quad (7)$$

where $\overline{N_H}$ is the mean N_H over rays in all directions (and thus contains all geometric considerations).

We now consider two limiting cases to bracket the plausible range of $L_{\text{halo}}/L_{\text{gal}}$ for the MSFR10 halo: a ‘‘point source’’ galaxy and a thin galaxy disk in a completely spherical halo. In the case of the point source, $N_H = \overline{N_H} = n_0/r_{\text{min}}$, so

$$(L_{\text{halo}}/L_{\text{gal}})_{\text{ps}} \sim 0.2/r_{\text{min,kpc}} \sim 0.1 \quad (8)$$

for $r_{\text{min}} = 2 \text{ kpc}$. In a real galaxy, L_{gal} is distributed over a disk much larger than r_{min} . Even if the halo becomes like an exponential atmosphere near the disk, the average N_H seen by light emitted from farther out in the disk will be smaller than near the center, so $(L_{\text{halo}}/L_{\text{gal}})_{\text{ps}}$ is higher than we expect in a real galaxy.

On the other hand, if L_{gal} is distributed over a thin, uniformly bright disk in the MSFR10 halo (i.e., extraplanar gas does not look like an exponential atmosphere near the disk), the $\overline{N_H}$ farther out in the disk will be lower than we expect from a real galaxy, so this situation provides a lower bound on $L_{\text{halo}}/L_{\text{gal}}$. To obtain $L_{\text{halo}}/L_{\text{gal}}$, we first find the $\overline{N_H}$ as a function of radius for a source emitting in the disk. We then integrate over the disk.

Consider a point source at a radius r in a disk of radius R (Figure 21). The total column density through the halo for each ray then depends on the angle θ , but one can see that the sum of $N_H(\theta)$ and $N_H(\pi + \theta)$ is equal to the projected column density $N_{H,\text{proj}}(r_p)$ at $r_p = r \sin \theta$. The mean $N_{H,\text{proj}}(r_p)$ occurs at $r_p = 2r/\pi$, since the mean of $\sin \theta = 2/\pi$ between 0 and π , so for $n(r) = n_0 r^{-2}$,

$$\overline{N_H}(r) = \frac{n_0}{2} \int_{r_p}^{\infty} dr \frac{1}{r^2} \frac{r}{\sqrt{r^2 - r_p^2}} = \frac{n_0 \pi^2}{8} \frac{1}{r} \quad (9)$$

For a uniformly bright, thin disk of total luminosity L_{gal} and inner and outer radii r_{min} (for consistency) and R , the total area is $\pi(R^2 - r_{\text{min}}^2)$ and the area element is $dA = 2\pi r dr$. Thus,

$$\begin{aligned} \left(\frac{L_{\text{halo}}}{L_{\text{gal}}}\right)_{\text{disk}} &= \frac{\sigma_{\text{ex}}\delta_{\text{DGR}}\varpi}{\pi(R^2 - r_{\text{min}}^2)} \int_{r_{\text{min}}}^R 2\pi r \left(\frac{\pi^2 n_0}{8} \frac{1}{r}\right) dr \\ &= r_{\text{min}} \frac{\pi^2}{4} \frac{(R - r_{\text{min}})}{(R^2 - r_{\text{min}}^2)} \left(\frac{L_{\text{halo}}}{L_{\text{gal}}}\right)_{\text{ps}} \end{aligned} \quad (10)$$

The Milky Way-sized disk galaxies in our sample have UV luminous disks with projected semimajor axes between 10–20 kpc. Taking this range for R , the scattered halo luminosity from our idealized disk is between 1/3

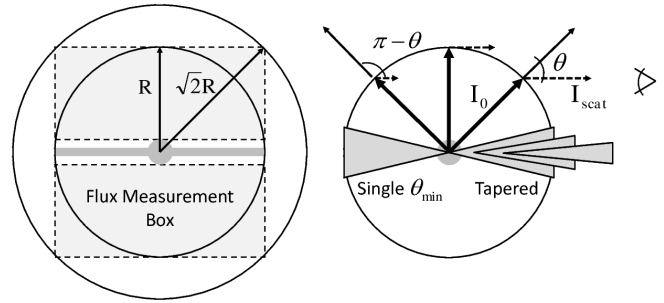


Figure 22. *Left:* The column density from the origin to the edge of the flux measurement box varies with angle, but the mean N_H occurs for a sphere with a radius in between the smallest circle to bound the box and the largest that fits inside. *Right:* The anisotropy in L_{halo} occurs because most light is scattered close to the incident angle. For an edge-on galaxy, light emerging from the galaxy close to the line of sight is strongly attenuated by the disk.

and 2/11 of that from a point source of the same L_{gal} at the center of the halo, or

$$(L_{\text{halo}}/L_{\text{gal}})_{\text{disk}} \sim 0.02 - 0.03 \quad (11)$$

The value can be scaled up or down if the disk is not uniformly bright, based on the concentration of light at each radius.

For the parameters above, we expect $0.02 \lesssim L_{\text{halo}}/L_{\text{gal}} \lesssim 0.1$. Considering differences in N_H , morphological type, disk size between galaxies of a similar absolute magnitude, and differences between σ_{ex} model curves, we expect the late-type galaxies to have

$$L_{\text{halo}}/L_{\text{gal}} \sim 0.04 - 0.1 \quad (12)$$

This ratio does not depend on the galaxy color.

6.3. Comparison to Observations

The total $L_{\text{halo}}/L_{\text{gal}}$ is not directly comparable to the measured values. First, we must determine the fraction of L_{halo} that we would see from a region of interest around a galaxy of a given inclination and disk thickness. This is important because scattering is forward-throwing (Draine 2003) and extinction in galaxy disks makes L_{gal} anisotropic. Second, we must correct the measured L_{gal} for extinction within the disk, as the galaxies in our sample are highly inclined.

6.3.1. Observable Fraction of L_{halo}

If we compute an isotropic luminosity from the measured UV fluxes ($4\pi d^2 F_{\text{halo}}$), it will underestimate the true L_{halo} for several reasons. The most obvious is that the flux measurement boxes (e.g., Figure 7) are smaller than the halo, but as most of the scattering occurs near the disk, inclination effects are more important. Due to extinction in the disk, more light emerges along the minor axis than near the major axis. A scattered photon is most likely to have a new trajectory at a small angle from the incident path (Draine 2003), so more of the total L_{halo} is visible from above the disk than from the side (if it could be separated from the non-scattered light).

For the MSFR10 halo we can estimate the amount of light that would be scattered into the line of sight for a given inclination, measurement region, and disk emission model. The ‘‘isotropic’’ halo luminosity derived from the

visible light we call $L_{\text{halo,vis}}$. $L_{\text{halo,vis}}$ underestimates the true L_{halo} for an edge-on galaxy and overestimates it for a face-on galaxy. For the remainder of this subsection, we consider a perfectly edge-on galaxy for the two limiting cases of a point source and a uniformly bright disk of radius R described above (Figure 21). $L_{\text{halo,vis}}$ is derived for a given flux measurement region by finding $\overline{N_H}$ for rays passing through that region and integrating over $d\sigma_{\text{scat}}/d\Omega$ from Draine (2003).

The boxes where we measure fluxes have finite width and height, but measure light from an infinite depth. For the MSFR10 halo, we can define a box and integrate numerically to evaluate N_H and $d\sigma_{\text{scat}}/d\Omega$, but with a few geometric simplifications we can make an instructive estimate. The box width is chosen to match the projected major axis of each galaxy, which corresponds to a radius R . The maximum height of the boxes in our sample is typically less than R , but as the halo fluxes drop below our sensitivity at lower heights, we make only a small error by assuming the distance from the top of the measurement boxes to the midplane of the galaxy is R . Since most scattering occurs at small radii, we can likewise truncate the depth and consider a cube with each side having a length $2R$ (the extension and truncation cause small errors in opposite directions). This geometry is shown in the left panel of Figure 22.

We can then identify a sphere that is similar enough to the cube that the $\overline{N_H}$ is approximately correct. This has the advantage of making N_H independent of angle and simplifying the integral over $d\sigma_{\text{scat}}/d\Omega$. The radius of the sphere can be obtained from the largest sphere that fits within the cube and the smallest one that bounds it (Figure 22). In the former case, the radius is R and in the latter it is $\sqrt{2}R$, so we take the mean N_H from the galactic center to the cube edge to be $N_H \approx n_0(1/r_{\text{min}} - 1/1.2R)$.

In this framework, the anisotropy in flux scattered into a given line of sight can be described in terms of an effective minimum polar angle θ_{min} for light emitted from the galaxy to escape its disk (Figure 22). For a chosen viewing angle, the amount of scattered light can be obtained by integrating $d\sigma_{\text{scat}}/d\Omega$ between θ_{min} and $\pi - \theta_{\text{min}}$ and multiplying by N_H (the integral over ϕ gives a factor of 2π). If the disk is uniformly thick at all radii and a gaseous disk extends beyond the UV-emitting region, θ_{min} is essentially constant, but one could also imagine a tapered disk (left and right halves of the circle shown on the right side of Figure 22). Based on typical N_H values in galaxy disks, θ_{min} in our sample is near $\theta_{\text{min}} \sim \pi/9$ (20°), but the extent of the range is not known. A real disk model is required and will be presented in a future work.

Using the WD01 SMC bar model and the Draine (2003) curve for the *uvm2* wavelength, $R = 10$ kpc and $r_{\text{min}} = 2$ kpc, and $\theta_{\text{min}} = \pi/9$, we find $L_{\text{halo,vis}}/L_{\text{gal}} \sim 0.001$ and 0.03 for the uniform disk and point source cases respectively. The lower bound is small because the flux measurement boxes are truncated at the disk width.

Considering the range in disk radii and uncertainty in θ_{min} , the geometric simplifications we made, and the different dust models, a plausible range for $L_{\text{halo,vis}}/L_{\text{gal}}$

for edge-on galaxies in the MSFR10 halo is

$$L_{\text{halo,vis}}/L_{\text{gal}} \sim 0.01 - 0.05 \quad (13)$$

When we numerically evaluate $L_{\text{halo,vis}}$ for extraction boxes of width $2R$ in the two limiting cases, we find values that fall within this range. The integral over $d\sigma/d\Omega$ increases for galaxies at lower inclination, but we actually expect a lower $L_{\text{halo,vis}}/L_{\text{gal}}$ for these systems because most scattering occurs at small radii, and the lower regions of the halo are seen in projection against the galaxy (where we do not measure halo flux).

6.3.2. Correcting for Extinction in the Measured L_{gal}

L_{gal} must be corrected because the observed flux is measured at a viewing angle with maximal extinction in the disk, whereas light escaping to the halo sees much less extinction. We correct for this by estimating the intrinsic UV luminosity and then estimating the extinction along the minor axis.

The UV flux absorbed by dust in the disk is reprocessed into the FIR, so one can use the FIR-to-UV flux ratio to estimate the UV extinction. As in Buat & Xu (1996), we use the sum of the IRAS $60 \mu\text{m}$ and $100 \mu\text{m}$ fluxes for the FIR flux. We adopt the fit in Buat et al. (1999) to star-forming galaxies (measured at 2000 \AA),

$$A_{\text{UV}} = 0.466(\pm 0.024) + 1.00(\pm 0.06) \log(F_{\text{FIR}}/F_{\text{UV}}) + 0.433(\pm 0.051) \log(F_{\text{FIR}}/F_{\text{UV}})^2 \quad (14)$$

and apply the extinction to the *uvm2* fluxes to obtain the intrinsic UV luminosity.

The light is attenuated as it exits the galaxy along the minor axis. We can estimate this factor from extinction corrections towards face-on galaxies (which also include any halo extinction, and are thus slightly too large). The extinction towards face-on disks depends on the galaxy type, luminosity, and the radius where it is measured. Based on Calzetti (2001) and references therein, the effective *B*-band extinction along the minor axis for late-type galaxies is perhaps $A_B = 0.4 - 0.6$ mag for an Sc or Sd galaxy and $A_B = 0.3 - 0.4$ mag for Sa and Sb galaxies. For Milky Way-type dust with $R_V = 3.1$, $A_{\text{UV}}/A_B = 2.4$, so L_{gal} as seen by the halo is about $0.7 - 1.7$ mag smaller than the intrinsic UV luminosity obtained from the Buat et al. (1999) correction. For SMC-type dust, $A_{\text{UV}}/A_B = 2.8$. Even within galaxies, it is not clear what dust model to use, as some have SMC-type dust (Calzetti et al. 1994) and others MW-type dust. The location of the dust relative to star forming regions may also play a role (Panuzzo et al. 2007), and starbursts tend to have higher A_B . As the difference is rather small, we adopt the MW-type dust value for the dust within the disk.

Thus,

$$L_{\text{gal,corr}} = 4\pi d^2 F_{\text{gal}} 10^{(A_{\text{UV,maj}} - A_{\text{UV,min}})/2.5} \quad (15)$$

where the “maj” and “min” subscripts refer to extinction through the disk along the major and minor axes respectively. Considering the scatter in the Buat et al. (1999) FIR-to-UV relation, reported differences in the extinction towards face-on galaxies, and the dependence of the extinction on the galaxy model (Calzetti 2001;

Table 7
Halo/Galaxy *uvm2* Luminosity Ratio

Galaxy	$uvm2 F_{\text{gal}}$ (10^{-11} erg s $^{-1}$ cm $^{-2}$ Å $^{-1}$)	F_{IR} (10^{-9} erg s $^{-1}$ cm $^{-2}$)	A_{UV} (mag)	A_B (mag)	$L_{\text{halo,vis}}$ ($10^8 L_{\odot}$)	$L_{\text{gal,corr}}$ ($10^8 L_{\odot}$)	$L_{\text{halo,vis}}/L_{\text{gal,corr}}$
NGC 24	6.72±0.02	0.17	0.95	0.5	0.23	4.8	0.05
NGC 891	3.09±0.07	6.16	5.06	0.5	0.71	75.	0.01
NGC 2841	10.0±0.03	0.54	1.37	0.4	0.58	22.	0.03
NGC 3079	9.82±0.01	4.81	3.39	0.6	1.4	113.	0.01
NGC 3628	8.32±0.04	5.51	3.78	0.6	1.2	81.	0.01
NGC 4088	1.13±0.01	2.41	2.56	0.5	0.41	73.	0.006
NGC 4388	3.00±0.01	1.08	3.07	0.4	0.37	43.	0.009
NGC 5301	2.53±0.02	0.35	2.17	0.5	0.54	24.	0.02
NGC 5775	2.69±0.01	2.13	3.93	0.5	1.9	165.	0.01
NGC 5907	7.23±0.03	1.55	2.57	0.4	2.7	61.	0.04
NGC 6503	14.6±0.01	1.12	1.69	0.5	0.009	4.5	0.002
NGC 6925	7.43±0.01	0.62	1.76	0.4	0.72	60.	0.01
NGC 7090	6.57±0.02	0.80	2.06	0.5	0.44	8.	0.06
NGC 7582	3.68±0.03	4.58	4.46	0.6	0.69	220.	0.003
UGC 6697	2.61±0.04	0.17	1.57	0.6	9.3	190.	0.05
UGC 11794	0.20±0.01	0.08	3.22	0.5	0.78	50.	0.02

Note. — Cols. (1) Galaxy name (2) *uvm2* galaxy flux (3) FIR flux (IRAS $F_{60\mu\text{m}} + F_{100\mu\text{m}}$) (4) A_{UV} estimated from the FIR flux using the Buat et al. (1999) relation, which we use as a correction from the edge-on perspective (5) A_B through the disk along the minor axis estimated from Calzetti (2001), which we use as a correction perpendicular to the disk. $A_{\text{UV}} = 2.4A_B$ for /citetaliasweingartner01 MW-type dust or $2.8A_B$ for SMC-type dust. We use MW-type dust here. (6) *uvm2* $L_{\text{halo,vis}}$ (7) *uvm2* $L_{\text{gal,corr}}$ (8) Halo-to-galaxy flux ratio.

Marcum et al. 2001), we suppose that $L_{\text{gal,corr}}$ is accurate to within 50% in most systems.

6.4. Comparison to Observed Fluxes

We can now compare the MSFR10 $L_{\text{halo,vis}}/L_{\text{gal}}$ to that derived from the UV data. Since we rely on the FIR data, we quote values for the 15 highly inclined Sa–Sc galaxies with FIR and *uvm2* data in Table 7. The other quantities in the table go into computing L_{gal} . For these galaxies, we find

$$(L_{\text{halo,vis}}/L_{\text{gal,corr}})_{\text{(obs)}} = 0.002 - 0.06 \quad (16)$$

This is remarkably similar to the range predicted by our MSFR10 extrapolation,

$$(L_{\text{halo,vis}}/L_{\text{gal}})_{\text{MSFR10}} = 0.01 - 0.05 \quad (17)$$

Galaxies with smaller inclination angles tend to have smaller values, as expected.

There are several comments worth making at this point. First, we expect $L_{\text{halo,vis}}/L_{\text{gal}}$ values of a few percent for a range of geometries and parameters because the MSFR10 A_V curve has a maximum column density of a few $\times 10^{20}$ cm $^{-2}$ for a realistic r_{min} , and integrating the Draine (2003) expression gives a cross-section of a few $\times 10^{-22}$ cm 2 . The errors we make through the various simplifying assumptions are smaller than the range from our upper/lower bound analysis.

Second, the observed $L_{\text{halo,i}}/L_{\text{gal}}$ values are consistent with the MSFR10 fit, but also any halo model that produces $N_H \sim 10^{20}$ cm $^{-2}$. The ratio by itself does not prove the MSFR10 model.

Third, there is intrinsic variation in the sample and $L_{\text{halo}}/L_{\text{gal}}$ does not necessarily follow H I halo mass (for example, NGC 891 has an unusually massive H I halo but a relatively low $L_{\text{halo}}/L_{\text{gal}}$). This could be due to variation in extinction through the disk, the location of star formation in the disk, and the difference in “real” r_{min} for each galaxy. A larger sample is also required to

rigorously determine whether the MSFR10 halo is valid within 15 kpc of the disk.

Finally, the results are shown for the *uvm2* data only, but we can also use the *GALEX* NUV and FUV with appropriate corrections and using the /citetaliasweingartner01 and Draine (2003) data for the right wavelengths. For example, for the FUV the Draine (2003) model and MSFR10 curve predict $L_{\text{halo,vis}}/L_{\text{gal}} \sim 0.02 - 0.09$. The Buat et al. (1999) correction is measured at longer wavelengths and so may not be valid, but blindly applying an extrapolation to the FUV band, we find $L_{\text{halo,vis}}/L_{\text{gal}} \sim 0.01 - 0.04$ for several galaxies where the FUV fluxes are well constrained.

6.5. Light Profile

We can also compare the expected light profile from MSFR10 to the observed fluxes. In Figure 23 we show the observed flux profiles for several of the galaxies in our sample with excellent data (boxes), where the fluxes have been normalized so that the y -axis shows the percentage of the total *observed* halo light seen in each bin. We have also overplotted a model based on the MSFR10 $n(r)$ using the same heights and projected bin sizes (albeit making a spherical approximation as for $L_{\text{halo,vis}}$ above). There is excellent agreement between the late-type galaxies in Figure 23, consistent with $n(r) = n_0 r^{-2}$ even at small radii.

It is worth noting that the profiles in Figure 23 do not depend on the galaxy luminosity, and the corresponding curves do not depend on the dust model (which affects total extinction). The profiles are thus a clean measure of how the density varies with radius, assuming a single type of dust and δ_{DGR} . A few of the early-type galaxies also show good agreement in Figure 23. The reason is unclear (most of the early-type galaxies in the sample prefer a shallower radial dependence), but in these galaxies the observed $L_{\text{halo}}/L_{\text{gal}} \sim 0.3 - 1.5$ before any correction for galactic extinction (the Buat et al. 1999,

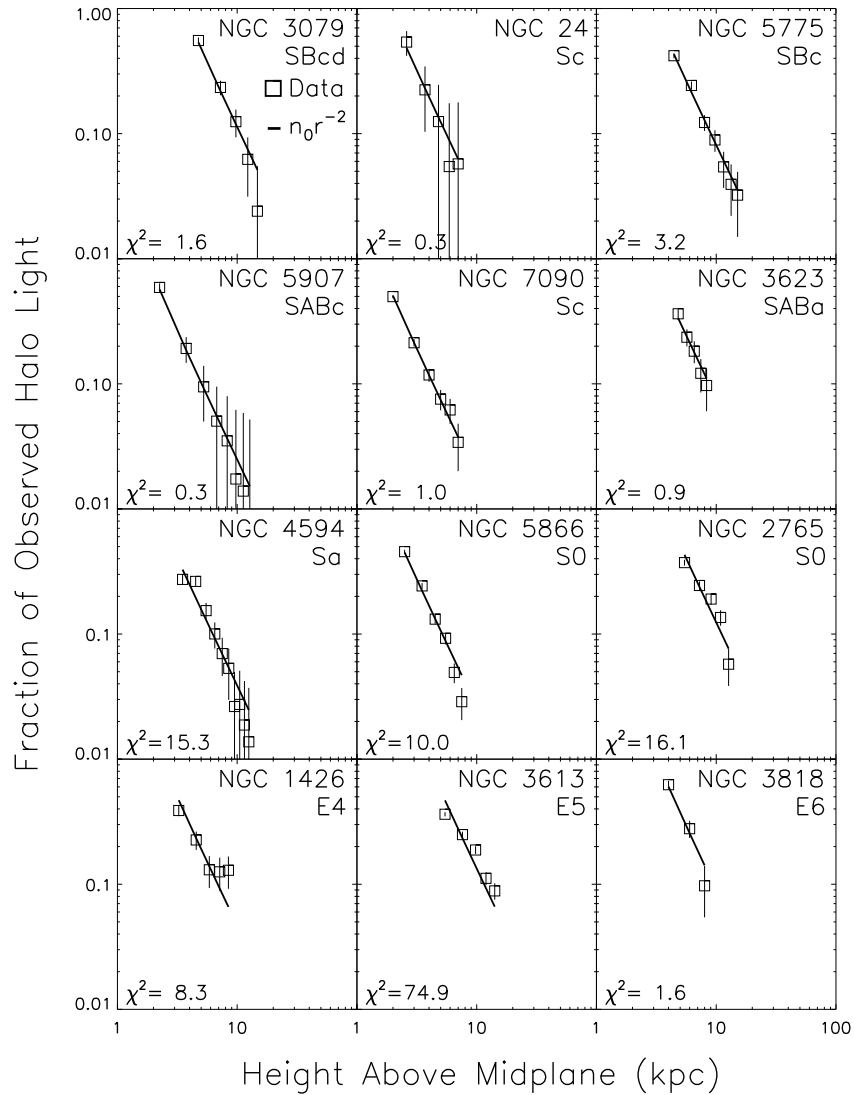


Figure 23. Measured halo light profiles for some of our sample (data points) and the prediction from the MSFR10 A_V fit (line). The lines are not fits to the data, but we compare them to the data with the χ^2 statistic shown in each panel.

fit is calibrated to star-forming galaxies), which is badly inconsistent with a scattered light origin.

The flux profiles and $L_{\text{halo,vis}}/L_{\text{gal}}$ derived from extrapolating the MSFR10 fit inwards are consistent with the observations.

6.6. Total N_H and Mass

If the MSFR10 halo extends to small radii, we can estimate the mass of dust-bearing gas within 20 kpc.

The N_H and mass implied by the MSFR10 curve depend on δ_{DGR} , which varies by location in the galaxies of the Local Group. For the Milky Way, $\delta_{\text{DGR}} \sim 1/100$, whereas in the Small Magellanic Cloud it is 5–10 times smaller (Gordon et al. 2003; Leroy et al. 2007). MSFR10 prefer SMC-type dust for the (outer) halo, but Ménard & Fukugita (2012) find that $\delta_{\text{DGR}} = 1/108$ for the halo dust outside 20 kpc. Thus, it seems likely that the true δ_{DGR} between 5–20 kpc is also about 1/100. This gives a maximum $N_H(r) \sim 3 \times 10^{20}/r_{\text{min,kpc}}$. For

$r_{\text{min}} = 2$ kpc, this is similar to typical sight lines out of the Milky Way at high latitudes, but these include disk material. It is about three times higher than N_H viewed out of the Lockman hole.

Column densities measured in projection towards edge-on extraplanar galaxies (e.g., Sancisi et al. 2008, and references therein) indicate maximum extraplanar $N_{H,\text{proj}}(r_p)$ of a few $\times 10^{20} \text{ cm}^{-2}$ (NGC 891 has a particularly massive halo with a maximum $N_H(r_p)$ about ten times higher). In the spherical halo model, at $r_p = 2$ kpc, $N_H(r_p) \approx 2.4 \times 10^{20} \text{ cm}^{-2}$, which is in agreement with these galaxies.

From the density profile we can measure the enclosed mass within a given radius (one could also integrate the projected column density implied by the MSFR10 ex-

tion curve over a visible area),

$$M(< r) = 4\pi\mu m_p \int r^2 n(r) dr \quad (18)$$

$$\sim 3.1 \times 10^7 (r_{\text{kpc}} - r_{\text{min,kpc}})$$

where μ is the mean atomic weight per particle and $n \sim 0.1 r_{\text{kpc}}^{-2} \text{cm}^{-3}$. Within 20 kpc, this yields $5 \times 10^8 M_\odot$ of gas, or several percent of the gas in the disk for a typical late-type galaxy.

6.7. Summary and Caveats

This section started from the proposition that if the extraplanar UV emission is a reflection nebula, we can use the fluxes to determine whether the UV emission is consistent with the same dust seen in extinction at larger radii. We found that the halo luminosities and flux profiles are indeed consistent with the MSFR10 fit within 20 kpc down to the edge of the thick disk, with a total dust-bearing gas mass of around $5 \times 10^8 M_\odot$ in this volume.

There are several potential weaknesses in this analysis. First, the results depend on the WD01 models and the Ménard & Fukugita (2012) δ_{DGR} for their halo dust, which determines n_0 (and thus N_H). N_H also depends on r_{min}^{-1} , so both L_{halo} and $M_{\text{gas}}(< r)$ in the halo depend on this value. Our choice of $r_{\text{min}} = 2$ kpc is based on physical considerations (albeit in an unphysical halo approximation), and perhaps validated by the extraplanar N_H measured in other galaxies. Still, a real halo model where the halo connects smoothly to the disk gas is required to explore this issue. Third, the L_{gal} that emerges from the disk depends on the disk thickness and density. We incorporated this as a θ_{min} above which light escapes into the halo, but a disk model is required to do a more careful computation. Finally, our corrections to the observed L_{gal} are based on the Buat et al. (1999) work and measurements of A_B through galaxy disks. There is a large scatter in both between galaxies, so our range of “measured” $L_{\text{halo}}/L_{\text{gal}}$ may not be conservative (i.e., wide) enough.

It is worth noting that most of the geometric simplifications we make introduce errors in N_H that are small compared to the range between the limiting cases we considered. A real model is required to go beyond this simple analysis. Likewise, the choice of SMC- or MW-type dust from the `/citetaliasweingartner01` models does not make a large difference if we adopt the Ménard & Fukugita (2012) δ_{DGR} for SMC-type halo dust.

7. DISCUSSION AND CONCLUSIONS

The main findings in this work are

1. Diffuse UV emission is ubiquitous around highly inclined late-type galaxies and in the outskirts of early-type galaxies.
2. In disk galaxies, the extent of this emission is 5–20 kpc (projected, no $\sin i$ correction) above the disk midplane. Halo UV luminosities (L_ν) range from 10^7 to a few $\times 10^8 L_\odot$ in the *Swift* and *GALEX* filters.
3. Close to the galaxy, the UV flux becomes higher near the projected disk center, but at larger minor

axis offsets (Figure 14) the emission is more uniform. There are differences in diffuse luminosity that do not correspond to differences in the SED.

4. The halo emission is not consistent with a classic stellar halo, but it is consistent with a reflection nebula produced by dust in the halo.
5. The distribution of this dust around the galaxy is consistent with extrapolating the MSFR10 fit to the mean extinction outside of 15–20 kpc to within a few kpc of the disk. This implies a typical dust-bearing gas mass of $\sim 5 \times 10^8 M_\odot$ for $\delta_{\text{DGR}} \sim 1/100$ within 20 kpc.
6. Unlike the MSFR10 detection of halo dust, which required averaging over extinction towards sources behind many galaxies, dust is detectable around individual galaxies in the UV, and possibly even substructure.

A definitive test of the reflection nebula hypothesis may be possible because the scattering cross-section is anisotropic (Draine 2003) and scattered light is highly polarized. Thus, in deep observations of highly inclined, but not edge-on, galaxies we expect a higher flux on one side of the galaxy than the other. The existing data for this sample are insufficient to make this measurement, and a larger sample with very little cirrus contamination is required. NGC 24 is a good candidate for inclusion in this sample, but the data are not deep enough. A UV polarimeter would determine whether the halo emission is highly polarized, but none is currently available, and the *uvw1* red leak indicates that the reflection nebula emission becomes dominated by a classical stellar halo somewhere between the NUV and *U* band.

Based on the existing evidence, we conclude that star-forming spiral galaxies produce reflection nebulas in their halos. There are a few important consequences:

First, the scattered-light spectrum could be used to constrain the metallicity with data in a few more filters. The fractional composition of the dust (e.g., the proportion of graphitic or silicate grains) determines the slope of the extinction curve in the FUV (e.g., Nozawa & Fukugita 2013). With additional measurements shortward of the 2175 Å bump, we could determine the slope (fits would be particularly sensitive to any data shortward of the *GALEX* FUV). Since the grain abundance depends on the gas metallicity, for galaxies with N_H measurements we could put a lower bound on the metal mass through δ_{DGR} .

Changes in the SEDs as a function of height would also determine how (or whether) dust evolves in the disk–halo interface. Extraplanar dust filaments are seen in NGC 891 (Rossa et al. 2004) and NGC 5775 (Howk 2009) that extend out to several kpc from the disk, but beyond this they find no dust structures despite having the sensitivity to do so. On the other hand, some dust filaments do extend to greater heights (Irwin & Madden 2006; McCormick et al. 2013), which may be related to galactic superwinds. In either case, at some point the dust becomes more diffuse, which may suggest that the dust is cosmologically old, that galaxies are inefficient at expelling dust to arbitrary radii, or that the disk–halo in-

terface is good at mixing small-scale structures into large ones.

Second, given that the Ménard & Fukugita (2012) δ_{DGR} beyond 20 kpc from the galaxy is close to the value within the Milky Way, if the dust is primarily in Mg II absorbers, the inferred mass suggests a comparable amount of hot and cold gas in galaxy halos within 20 kpc (for examples of hot mass, see Bregman & Pildis 1994; Strickland et al. 2004; Li & Wang 2013). This may be true at larger radii as well: MSFR10 estimate a total dust mass within the virial radius of $5 \times 10^7 M_{\odot}$ (measured outside 20 kpc), corresponding to a gas mass of $M_{\text{gas}} \sim 6 \times 10^9 M_{\odot}$. Anderson et al. (2013) estimate a total hot mass within 50 kpc of late-type galaxies of about $5 \times 10^9 M_{\odot}$. This balance is consistent with hydrodynamic cosmological simulations in Cen (2013).

Another possibility is that some of the dust is hosted in the hot gas itself, which may help the hot gas cool. The discovery of diffuse intergalactic dust in galaxy clusters (Chelouche et al. 2007), which are filled with comparatively dense, hot gas, indicates that dust must be accreted regularly into these systems because of the sputtering times (McGee & Balogh 2010). However, in the more tenuous hot halos of galaxies, grains can survive for considerably longer.

Third, variations in flux along the projected major axis with no corresponding change in SED (Figure 14 and seen in several other galaxies) beyond several kpc from the disk may trace denser clouds and thus gaseous structures in external galaxies. For nearby galaxies, deep UV exposures could probe the gas structure of the halo on spatial scales of a few kpc. However, it is also possible that the differences arise from anisotropic illumination of the halo by the disk, so a real galaxy-halo model is required for further study. Another intriguing possibility is to look for satellite galaxies through variations in the SED. Galaxies like NGC 5907 have such uniform UV halo SEDs (Figure 14) that bins with markedly different SEDs may identify compact halo structures. However, high resolution optical follow-up would be necessary to rule out point sources or background galaxies.

If the SEDs can be connected to dust properties, UV photometry of galaxy halos will be a powerful way to study individual galaxies with relatively short exposures compared to those required for true spectroscopy.

Fourth, if the UV emission is a proxy for halo gas then it may be much easier to detect cool extraplanar gas within ~ 20 kpc of the disk using UV imaging rather than radio interferometry, which provides more information at the cost of much longer integration times in the large arrays needed to achieve arcsecond resolution.

Finally, the detection of the diffuse UV halos indicates that studies of diffuse UV emission (besides the Galactic cirrus) are possible with *Swift*. We have examined potential contamination sources in detail, and the agreement between the *Swift* and *GALEX* fluxes strongly indicates that we see intrinsic emission from the galaxy halo. It is worth noting that the correction needed to make the *uvw1* a true “UV” flux (in the halo) appears to be similar for all of the late-type galaxies in our sample, and the *UBV* filters aboard *Swift* are also sensitive enough to constrain the stellar halo luminosity. Thus, one can in principle use *Swift* observations without *GALEX* data,

and there are a number of galaxies with deep *Swift* data with shallow or missing *GALEX* data.

The authors thank Eric Bell and Alice Breeveld for helpful input, and Adolf Witt for pointing out that the “UV bump” is a purely absorptive feature and cannot be used to distinguish dust models via scattered spectra. The authors thank the referee for substantial and detailed comments that greatly improved the paper. EHK was supported by NASA ADAP grant #061951.

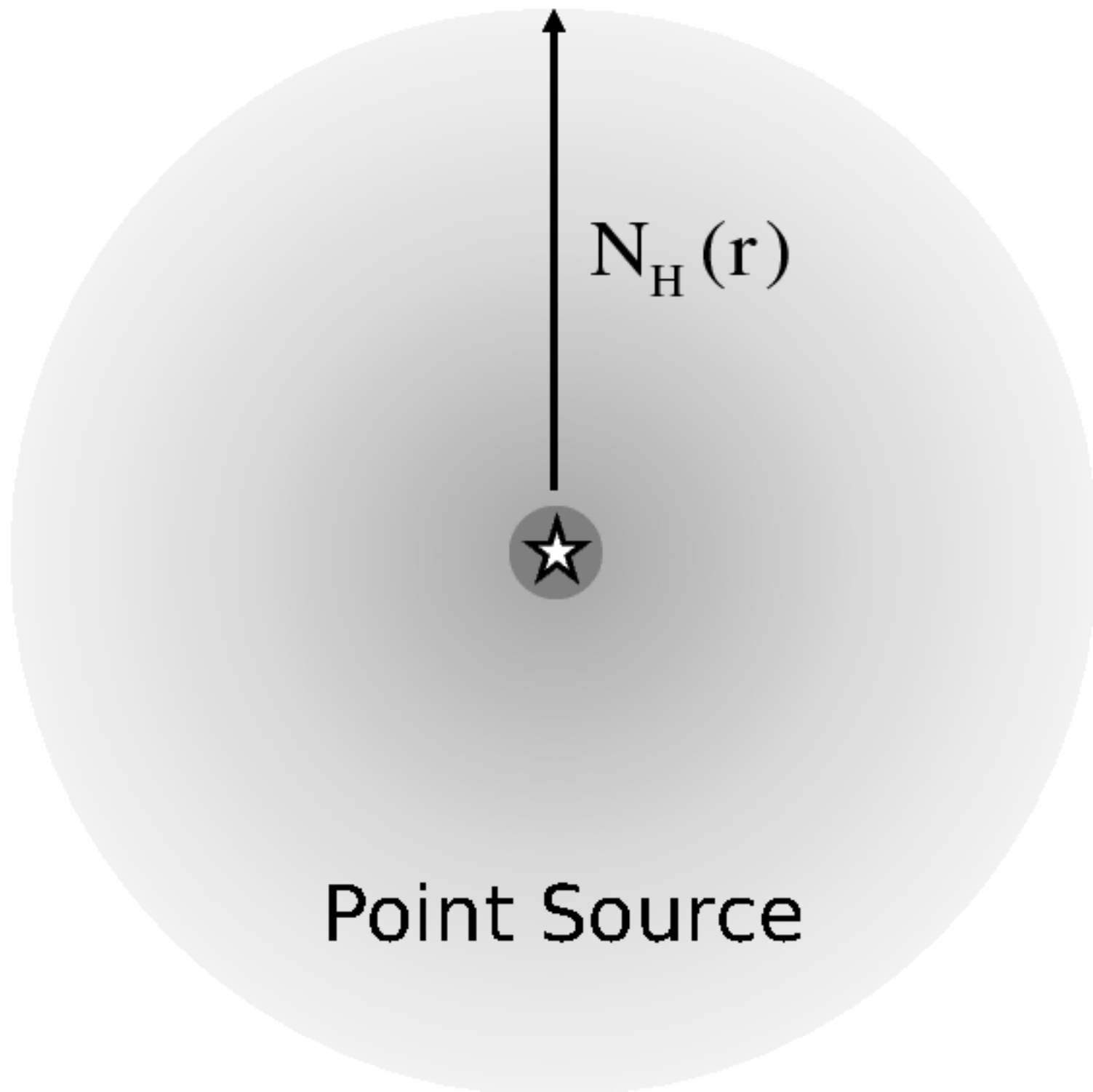
This research has made use of data and/or software provided by the High Energy Astrophysics Science Archive Research Center (HEASARC), which is a service of the Astrophysics Science Division at NASA/GSFC and the High Energy Astrophysics Division of the Smithsonian Astrophysical Observatory.

Facilities: GALEX, Swift

REFERENCES

- Abazajian, K. N., Adelman-McCarthy, J. K., Agüeros, M. A., et al. 2009, *ApJS*, 182, 543
- Anderson, M. E., Bregman, J. N., & Dai, X. 2013, *ApJ*, 762, 106
- Andriesse, C. D., Piersma, T. R., & Witt, A. N. 1977, *A&A*, 54, 841
- Bell, E. F., & de Jong, R. S. 2001, *ApJ*, 550, 212
- Bertin, E., & Arnouts, S. 1996, *A&AS*, 117, 393
- Bolzonella, M., Miralles, J.-M., & Pelló, R. 2000, *A&A*, 363, 476
- Breeveld, A. A., Landsman, W., Holland, S. T., et al. 2011, in *American Institute of Physics Conference Series*, Vol. 1358, American Institute of Physics Conference Series, ed. J. E. McEney, J. L. Racusin, & N. Gehrels, 373–376
- Breeveld, A. A., Curran, P. A., Hoversten, E. A., et al. 2010, *MNRAS*, 406, 1687
- Bregman, J. N. 1980, *ApJ*, 236, 577
- . 2007, *ARA&A*, 45, 221
- Bregman, J. N., & Pildis, R. A. 1994, *ApJ*, 420, 570
- Brown, P. J., Roming, P. W. A., Milne, P., et al. 2010, *ApJ*, 721, 1608
- Buat, V., Donas, J., Milliard, B., & Xu, C. 1999, *A&A*, 352, 371
- Buat, V., & Xu, C. 1996, *A&A*, 306, 61
- Burgdorf, M., Ashby, M. L. N., & Williams, R. 2007, *ApJ*, 668, 918
- Burstein, D., Bertola, F., Buson, L. M., Faber, S. M., & Lauer, T. R. 1988, *ApJ*, 328, 440
- Calzetti, D. 2001, *PASP*, 113, 1449
- Calzetti, D., Bohlin, R. C., Gordon, K. D., Witt, A. N., & Bianchi, L. 1995, *ApJ*, 446, L97
- Calzetti, D., Kinney, A. L., & Storchi-Bergmann, T. 1994, *ApJ*, 429, 582
- Carney, B. W., Latham, D. W., & Laird, J. B. 1989, *AJ*, 97, 423
- Cen, R. 2013, *ApJ*, 770, 139
- Chelouche, D., Koester, B. P., & Bowen, D. V. 2007, *ApJ*, 671, L97
- Code, A. D., & Welch, G. A. 1979, *ApJ*, 228, 95
- Coleman, G. D., Wu, C.-C., & Weedman, D. W. 1980, *ApJS*, 43, 393
- Draine, B. T. 2003, *ApJ*, 598, 1017
- . 2004, *Origin and Evolution of the Elements*, 317
- Fraternali, F., van Moorsel, G., Sancisi, R., & Oosterloo, T. 2002, *AJ*, 123, 3124
- Fukugita, M., Shimasaku, K., & Ichikawa, T. 1995, *PASP*, 107, 945
- Garcia-Burillo, S., Guelin, M., Cernicharo, J., & Dahlem, M. 1992, *A&A*, 266, 21
- Gehrels, N., Chincarini, G., Giommi, P., et al. 2004, *ApJ*, 611, 1005
- Gil de Paz, A., Boissier, S., Madore, B. F., et al. 2007, *ApJS*, 173, 185
- Gordon, K. D., Clayton, G. C., Misselt, K. A., Landolt, A. U., & Wolff, M. J. 2003, *ApJ*, 594, 279
- Hodges-Kluck, E. J., & Bregman, J. N. 2013, *ApJ*, 762, 12
- Howk, J. C. 2009, *ArXiv e-prints*, arXiv:0904.4928

- Howk, J. C., & Savage, B. D. 2000, *AJ*, 119, 644
- Irwin, J. A., & Madden, S. C. 2006, *A&A*, 445, 123
- Jenkins, E. B. 2004, *Origin and Evolution of the Elements*, 336
- Jeong, H., Bureau, M., Yi, S. K., Krajinović, D., & Davies, R. L. 2007, *MNRAS*, 376, 1021
- Kamphuis, P. 2008, PhD thesis, PhD Thesis, University of Groningen, (2008)
- Kennicutt, Jr., R. C. 1998, *ApJ*, 498, 541
- Kinney, A. L., Calzetti, D., Bohlin, R. C., et al. 1996, *ApJ*, 467, 38
- Kotulla, R., Fritze, U., Weilbacher, P., & Anders, P. 2009, *MNRAS*, 396, 462
- Lee, S.-W., Seaquist, E. R., Leon, S., García-Burillo, S., & Irwin, J. A. 2002, *ApJ*, 573, L107
- Lequeux, J., Fort, B., Dantel-Fort, M., Cuillandre, J.-C., & Mellier, Y. 1996, *A&A*, 312, L1
- Leroy, A., Bolatto, A., Stanimirovic, S., et al. 2007, *ApJ*, 658, 1027
- Li, J.-T., & Wang, Q. D. 2013, *MNRAS*, 428, 2085
- Marcum, P. M., O'Connell, R. W., Fanelli, M. N., et al. 2001, *ApJS*, 132, 129
- Martin, D. C., Fanson, J., Schiminovich, D., et al. 2005, *ApJ*, 619, L1
- McCormick, A., Veilleux, S., & Rupke, D. S. N. 2013, *ApJ*, 774, 126
- McGee, S. L., & Balogh, M. L. 2010, *MNRAS*, 405, 2069
- Ménard, B., & Fukugita, M. 2012, *ApJ*, 754, 116
- Ménard, B., Scranton, R., Fukugita, M., & Richards, G. 2010, *MNRAS*, 405, 1025
- Monet, D. G., Levine, S. E., Canzian, B., et al. 2003, *AJ*, 125, 984
- Morrissey, P., Conrow, T., Barlow, T. A., et al. 2007, *ApJS*, 173, 682
- Nozawa, T., & Fukugita, M. 2013, *ApJ*, 770, 27
- Oosterloo, T., Fraternali, F., & Sancisi, R. 2007, *AJ*, 134, 1019
- Panuzzo, P., Granato, G. L., Buat, V., et al. 2007, *MNRAS*, 375, 640
- Parnovsky, S. L., Izotova, I. Y., & Izotov, Y. I. 2013, *Ap&SS*, 343, 361
- Poole, T. S., Breeveld, A. A., Page, M. J., et al. 2008, *MNRAS*, 383, 627
- Putman, M. E., Peek, J. E. G., & Jounge, M. R. 2012, *ARA&A*, 50, 491
- Rice, W., Lonsdale, C. J., Soifer, B. T., et al. 1988, *ApJS*, 68, 91
- Roming, P. W. A., Kennedy, T. E., Mason, K. O., et al. 2005, *Space Sci. Rev.*, 120, 95
- Roming, P. W. A., Koch, T. S., Oates, S. R., et al. 2009, *ApJ*, 690, 163
- Rossa, J., Dettmar, R.-J., Walterbos, R. A. M., & Norman, C. A. 2004, *AJ*, 128, 674
- Sackett, P. D., Morrisoni, H. L., Harding, P., & Boroson, T. A. 1994, *Nature*, 370, 441
- Sancisi, R., Fraternali, F., Oosterloo, T., & van der Hulst, T. 2008, *A&A Rev.*, 15, 189
- Schechter, P. 1976, *ApJ*, 203, 297
- Schlafly, E. F., & Finkbeiner, D. P. 2011, *ApJ*, 737, 103
- Schlegel, D. J., Finkbeiner, D. P., & Davis, M. 1998, *ApJ*, 500, 525
- Skrutskie, M. F., Cutri, R. M., Stiening, R., et al. 2006, *AJ*, 131, 1163
- Strickland, D. K., Heckman, T. M., Colbert, E. J. M., Hoopes, C. G., & Weaver, K. A. 2004, *ApJS*, 151, 193
- Sujatha, N. V., Murthy, J., Suresh, R., Conn Henry, R., & Bianchi, L. 2010, *ApJ*, 723, 1549
- Tumlinson, J., Thom, C., Werk, J. K., et al. 2013, *ApJ*, 777, 59
- Tzanavaris, P., Hornschemeier, A. E., Gallagher, S. C., et al. 2010, *ApJ*, 716, 556
- Weingartner, J. C., & Draine, B. T. 2001, *ApJ*, 548, 296
- Westmeier, T., Braun, R., Brüns, C., Kerp, J., & Thilker, D. A. 2007, *New. A. Rev.*, 51, 108
- Wyder, T. K., Martin, D. C., Schiminovich, D., et al. 2007, *ApJS*, 173, 293
- Yi, S. K., Lee, J., Sheen, Y.-K., et al. 2011, *ApJS*, 195, 22
- Yoachim, P., & Dalcanton, J. J. 2006, *AJ*, 131, 226
- Zaritsky, D. 1994, *AJ*, 108, 1619



$$N_H(r)$$

Point Source

NGC 5775

